



Research paper

Analysis of the water-exit cavity evolution and motion characteristics of an underwater vehicle under the effect of floating ice

Hao Wang^a, Zhengui Huang^{a,*}, Xiaowei Cai^b, Xiangyan Liu^a, Zhihua Chen^a, Xiaodong Na^a

^a National Key Laboratory of Transient Physics, Nanjing University of Science and Technology, Nanjing, 210094, China

^b National Key Laboratory of Hydrodynamics, China Ship Scientific Research Center, Wuxi, 214082, China

ARTICLE INFO

Keywords:

Floating ice

Vehicle

Water-exit cavity

Motion characteristics

ABSTRACT

In high latitudes during winter, the icing period is inevitable. Expanding submarine-launched marine equipment in a low-temperature ice environment holds significant engineering value. However, the existence of floating ice will unavoidably increase the nonlinearity of the submarine-launched vehicle during the water-exit process. The dynamic fluid interaction module (DFBI) and the multi-overlapping grid method were used to establish 6-degree-of-freedom motion models for the floating ice and the vehicle. By comparing and analyzing the underwater and cross-water stages of the vehicle under varying quantities, thicknesses and shapes of floating ice, the mechanisms of the influence of floating ice on the water-exit cavity evolution and the motion characteristics of the vehicle were explored. The findings indicate that the floating ice causes the cavity on the near-ice side to bend and the free liquid surface to form a "circular arch" shape, resulting in premature wetting of the vehicle. Moreover, it reduces the wetting degree of the vehicle's surface away from the ice side. In the direction of the ice, the hydrodynamic force and moment acting on the vehicle are stronger, with more drastic changes and longer fluctuation durations, resulting in more severe horizontal velocity and attitude angle deviations affected by floating ice.

1. Introduction

Submarine-launched vehicles have gained increasing attention for their advantages, such as excellent concealment and strong maneuverability. The process of high-speed water exit involves the underwater stage and the cross-water stage, which encompasses various factors, including cavitation flow, multiphase coupling of vapor/liquid/gas, medium mutation, as well as turbulence and fluid-solid coupling characteristics. These aspects contribute to the water-exit process's high instability and strong nonlinearity (Quan et al., 2008; Brennen, 2013; Huang et al., 2014; Xu et al., 2019; Sun et al., 2019), which directly affect the motion state and control performance of the vehicle.

The polar region is regarded as one of the most strategically valuable areas in the world due to its unique geographical location and environmental conditions. Affected by global warming, some icebergs in the Arctic, which are rich in mineral resources such as oil and gas, are gradually melting. As a result, the available sea areas are gradually increasing, making it possible to exploit polar resources and bringing opportunities and challenges to Arctic countries (Guo and Sun, 2020). Whether it is the resource-rich Arctic or high-latitude regions like the

Bohai Sea and the Yellow Sea during winter, the presence of floating ice and ice-water mixture on the low-temperature sea surface is inevitable (Zhang et al., 2019; Nam et al., 2013; Moore et al., 2021). While sea ice can provide better concealment for submarine-launched vehicles, it also introduces a more complex process of crossing the gas-water interface, thereby affecting the vehicle's motion state and the secondary adjustment after exiting the water. Consequently, researching submarine-launched marine equipment in a low-temperature ice environment holds significant engineering research value and practical significance.

Numerous scholars have researched cavitation flow and water-exit problems from theoretical aspects such as mathematical models (Logvinovich, 1969; Brennen, 1995; Kunz et al., 2000; Moyo and Greenhow, 2000; Korobkin, 2013). However, due to various limitations, accurately describing the unsteady cavitation phenomenon in high-speed water-exit processes remains challenging. Advancements in industrial-level and experimental equipment have facilitated the use of experimental research to observe and analyze water exit phenomena, leading to more diverse studies. Experimental research on the low-speed vertical and inclined water-exit processes of slender bodies was carried out by Zhao

* Corresponding author.

E-mail address: hgzkeylab@njust.edu.cn (Z. Huang).

et al. (2016) and Fu et al. (2018). The findings revealed that the attitude and trajectory changes of slender bodies are not non-linearly related to the initial inclination angle but rather to the closure position of the shoulder cavity. The mechanisms involved in the formation, development, and collapse of the water-exit cavity were also investigated. Chen et al. (2021) investigated the effects of projectile head shape and launch speed on cavity shedding and projectile stability using a self-designed underwater launch platform. Using high-speed photography to conduct experiments, Takamure and Uchiyama (2021) proposed two methods for estimating water mass during the vertical water-exit process of solid particles based on images captured from orthogonal directions. Zhao et al. (2022) conducted experimental studies on the flow characteristics and pressure loads of warheads, including cone head, hemispheric head, and swinging conical head projectiles, during the water-exit process. It was found that the initial, developmental, and collapse stages of the corresponding cavity for different head projectiles have significant differences, and the pressure change process is different from the collapse time of the three water columns.

In recent years, the continuous progress of numerical calculation methods has enabled scholars to analyze water-exit problems with greater precision and depth. Hao et al. (2019) utilized the Boltzmann method to study the changes in the free liquid surface of a small ball during the water-exit process at different Froude numbers. Chen et al. (2021) conducted a numerical simulation study employing large eddy simulation to examine the cavitation flow of a submarine-launched vehicle during water exit under varying conditions of depths, velocities, and angles of attack. They comprehensively summarized the evolution process of the cavity, turbulent structures, and pressure characteristics. Nguyen et al. (2022) numerically studied the vertical and oblique water-exit processes of a vehicle under different cavitation numbers and angles. It was revealed that the collapse of the cavity induces high-pressure pulsations on the surface of the vehicle. Furthermore, more complicated parameter circumstances, like ventilated water exit (Liu et al., 2017), continuous water exit (Xu et al., 2019), parallel water exit (Shi et al., 2022), and water exit under wave action (Sun et al., 2022), have been taken into account in certain numerical water-exit investigations.

Currently, research on water exit is mostly limited to open water environments without obstacles, with limited consideration for cross-media studies involving ice-water mixture (Wang et al., 2022a; Wang et al., 2022b; Cui et al., 2023). The research on water exit in a low-temperature ice environment is still in its nascent stages. The vertical and oblique launch of underwater vehicles through a mixed environment of brash ice and water had been investigated (Zhang et al., 2021; Sun et al., 2022; You et al., 2022). It was found that the floating ice altered the intensity and range of cavity collapse splashing, causing substantial fluctuations in pressure on the vehicle's surface, and consequently affecting its movement trajectory. Wang et al. (2023) used the CFD-DEM method to comparatively investigate the process of a high-speed submarine-launched vehicle penetrating water (without floating ice) and ice-water mixture. The findings revealed that the floating ice accelerates the collapse of the attached cavity, and causes the vehicle to be subjected to a severe fluctuating alternating load and lasts for a longer time, which changes the trajectory characteristics of the vehicle, reducing its motion stability and intensifying trajectory deviation.

Stress concentration will occur during the process of submarine-launched vehicles breaking through the ice cover, which is easy to lead to structural damage, posing a threat to safety and seriously affecting ballistic stability. Therefore, "floating ice gap" and "ice crack" are preferred for underwater launching in a low-temperature ice environment. The presence of floating ice near the water-exit point creates a unique mechanical environment for submerged vehicles, leading to differences in the cavity evolution and motion characteristics compared with those without ice. However, the exact mechanisms of the influence of floating ice on this process remain unclear. Conducting experimental

investigations into the water-exit process in low temperatures with floating ice poses significant challenges due to the harsh environmental conditions and high technical difficulty and cost. In this study, numerical simulations were employed to compare the influence mechanisms of no ice versus different quantities, thicknesses and shapes of floating ice on the cavity evolution and motion characteristics of an underwater vehicle during the high-speed water exit. The results can provide some reference value for the study of submarine-launched vehicles in low-temperature ice environments.

2. Numerical methodology

2.1. Governing equations

Ignoring the compressibility and heat conduction effect of water, based on the Reynolds-averaged Navier-Stokes (RANS) equation, the multiphase flow field structure and fluid dynamics are obtained by solving the mass conservation equation and the momentum conservation equation:

$$\frac{\partial}{\partial t}(\rho_m) + \frac{\partial}{\partial x_i}(\rho_m u_i) = 0 \quad (1)$$

$$\frac{\partial}{\partial t}(\rho_m u_i) + \frac{\partial}{\partial x_j}(\rho_m u_i u_j) = -\frac{\partial P}{\partial x_i} + \frac{\partial}{\partial x_i} \left[(\mu_m + \mu_t) \left(\frac{\partial u_i}{\partial x_j} + \frac{\partial u_j}{\partial x_i} \right) \right] + \rho_m g_i \quad (2)$$

Where ρ_m is the mixture's density, u_i and g_i denote orthogonal component of the fluid velocity vector u and the volumetric gravity in the direction i in the Cartesian coordinate system, respectively. P is flow pressure, μ_m and μ_t are the dynamic viscosity of the mixing medium and turbulent viscosity corresponding to the turbulence model, respectively.

2.2. Turbulence model

The SST $k-\omega$ turbulence model combines the advantages of both the $k-\omega$ turbulence model and the $k-\varepsilon$ turbulence model (Menter, 1994), with high accuracy in predicting flow near the wall, accurate description of large-scale vortex and turbulent diffusion, as well as good robustness.

The eddy viscosity coefficient is defined as:

$$\mu_t = \rho_m k T \quad (3)$$

Where T is turbulent time scale.

The transport equation of turbulent kinetic energy k and unit dissipation rate ω is:

$$\frac{\partial}{\partial t}(\rho_m k) + \frac{\partial}{\partial x_i}(\rho_m k u_i) = \frac{\partial}{\partial x_i} \left[(\mu + \sigma_k \mu_t) \frac{\partial k}{\partial x_i} \right] + P_k - \rho_m \beta^* f_{\beta^*} (\omega k - \omega_0 k_0) + S_k \quad (4)$$

$$\frac{\partial}{\partial t}(\rho_m \omega) + \frac{\partial}{\partial x_i}(\rho_m \omega u_i) = \frac{\partial}{\partial x_i} \left[(\mu + \sigma_\omega \mu_t) \frac{\partial \omega}{\partial x_i} \right] + P_\omega - \rho_m \beta f_{\beta} (\omega^2 - \omega_0^2) + S_\omega \quad (5)$$

Where σ_k and σ_ω are the model coefficients, P_k and P_ω denote the generation items, f_{β^*} and f_{β} are the correction factors, k_0 and ω_0 represent the environmental turbulence values to prevent turbulence attenuation. S_k and S_ω are user-defined source terms.

2.3. VOF model

As it involves natural cavitation near the wall of the vehicle, the multiphase interaction and unsteady change of the intersecting interface need to be taken into account. The volume of fluid (VOF) model is selected to capture the distribution and movement of the immiscible interface. The volume fractions of water, air and vapor are represented by α_l , α_g and α_v , respectively. The sum of the volume fractions of all

Table 1
Calculation conditions of different floating ice quantities.

| Case number | Condition/Case name | Velocity |
|-------------|---------------------|----------|
| 1 | 0 ice | 35 m/s |
| 2 | 1 ice | 35 m/s |
| 3 | 2 ice | 35 m/s |
| 4 | 3 ice | 35 m/s |
| 5 | 4 ice | 35 m/s |

phases in a grid cell is 1:

$$\alpha_l + \alpha_g + \alpha_v = 1 \quad (6)$$

The density and dynamic viscosity of the mixed medium are defined as follows:

$$\rho_m = \alpha_l \rho_l + \alpha_g \rho_g + \alpha_v \rho_v \quad (7)$$

$$\mu_m = \alpha_l \mu_l + \alpha_g \mu_g + \alpha_v \mu_v \quad (8)$$

Where ρ_l, ρ_g, ρ_v and μ_l, μ_g, μ_v denote the density and the dynamic viscosity of water, air and vapor, respectively.

2.4. Cavitation model

The Schnerr-Sauer cavitation model scales the bubble growth rate and collapse rate of multicomponent materials with high computational efficiency (Schnerr and Sauer., 2001). The mass transfer description of the phase transition between the water phase and the vapor phase in the Schnerr-Sauer cavitation model is described as follows:

$$\begin{cases} \frac{\partial}{\partial t}(\rho_v \alpha_v) + \frac{\partial}{\partial x_i}(\rho_v \alpha_v u_i) = R_e - R_c \\ R_e = F_{vap} \frac{\rho_l \rho_v}{\rho_w} \alpha(1 - \alpha) \frac{3}{R_B} \sqrt{\frac{2}{3} \frac{P_v - P}{\rho_l}}, P < P_v \\ R_c = F_{cond} \frac{\rho_l \rho_v}{\rho_m} \alpha(1 - \alpha) \frac{3}{R_B} \sqrt{\frac{2}{3} \frac{P - P_v}{\rho_l}}, P > P_v \\ R_B = \left(\frac{\alpha}{1 - \alpha} \frac{3}{4\pi n_b} \right)^{\frac{1}{3}} \end{cases} \quad (9)$$

Where F_{vap} and F_{cond} are the evaporation and condensation coefficients, respectively. R_B is the radius of the gas nucleus, n_b is the number of gas nuclei per unit volume of fluid, $P_v = 610.47$ Pa (Saturated vapor pressure of water at 0 °C)

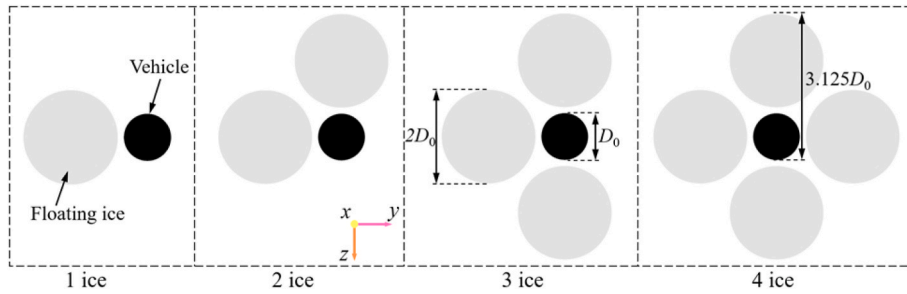


Fig. 1. Distribution of the vehicle and floating ice at the initial moment (top view).

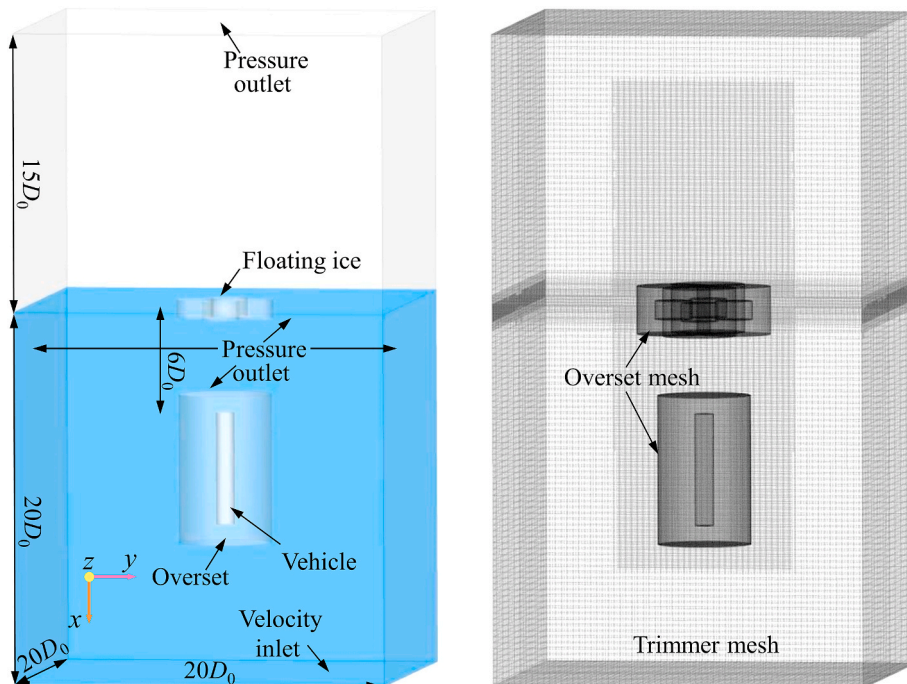


Fig. 2. Schematic of the boundary conditions and the mesh.

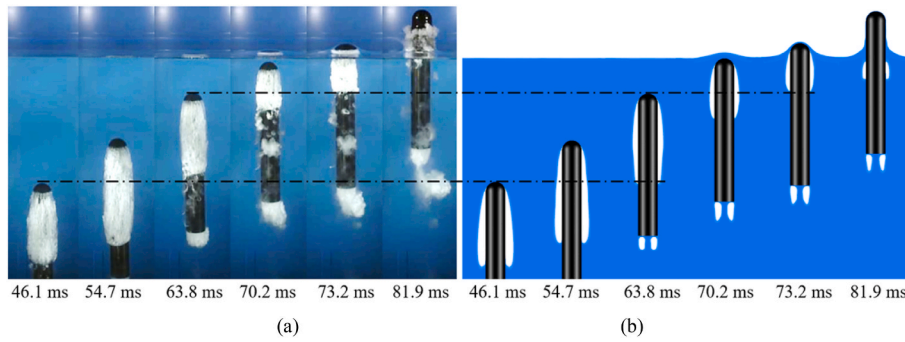


Fig. 3. Comparison of cavity evolution between (a) the experiment result and (b) the numerical simulation.

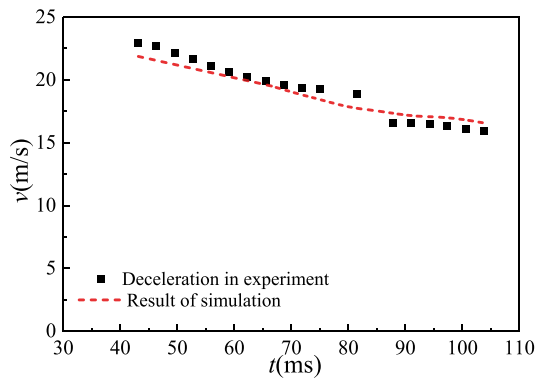


Fig. 4. Comparison of velocity of the vehicle.

2.5. Numerical model setup

The vehicle is an aluminum cylinder with a length-diameter ratio of 6, and the diameter D_0 is 12.65 mm. To facilitate the study of mechanism, the selection of the shape and thickness of floating ice is associated with the vehicle, a cylindrical shape is used for simplified characterization, with a diameter of $2D_0$, a height of D_0 , and a density of 920 kg/m^3 . The initial velocity of the vertical water exit of the vehicle is 35 m/s . At the initial moment, the floating ice is positioned around the water-exit point of the vehicle, with an initial radial gap of $0.125 D_0$ from the vehicle, and the floating ice is in a state of equilibrium between buoyancy and its gravity.

In order to explore the influence mechanism of different quantities of floating ice on the cavity evolution and motion characteristics of an underwater vehicle during the high-speed water exit, based on the condition of no ice, 1, 2, 3 and 4 ice floes are arranged around the water-exit point for comparative study, as shown in Table 1. The distribution (top view) of 1, 2, 3 and 4 ice floes at the initial moment is presented in

Fig. 1.

Fig. 2 displays the calculation domain and the grid division. The dimensions of the calculation domain are labeled as $20 D_0$ in length, $20 D_0$ in width, and $35 D_0$ in height. The launch depth of the vehicle is $6 D_0$. The water surface sits at a distance of $15 D_0$ from the top of the calculation domain, with the remaining upper section being filled with air. Around the periphery and atop the calculation domain, pressure outlets have been designated, while the bottom has been assigned as the velocity inlet. The surfaces of both the vehicle and the floating ice are designated as walls. The ground coordinate system has the x-axis vertically down, the y-axis horizontally to the right, and the z-axis perpendicular to the Oxy plane and obeys the right-hand spiral rule. At the commencement of the process, the axes of the projectile coordinate system, with the center of mass of the vehicle as the origin, are in the same direction as the ground coordinate system.

The trimmer unit is used for meshing, and the mesh of the moving area of the vehicle and the area near the free surface is encrypted to ensure the capture of the flow field details. To more accurately exchange data between fluid and solid through interpolation during the movement of the floating ice and the vehicle, 6-degree-of-freedom motion models of the floating ice and the vehicle are established by using the dynamic fluid interaction model (DFBI) and multi-overlapping grid method. During the calculation process, the background grid remains stationary, and the overlapping grid moves together with the solid.

The numerical simulation was carried out based on the computational fluid dynamics software STAR-CCM+. Second-order implicit time discretization was selected, with a second-order upwind scheme for the convection term, a second-order central difference scheme for the diffusion term, and the SIMPLE algorithm (Semi-Implicit Method for Pressure-Linked Equations) based on pressure for the separation solver. The algebraic multigrid method (AMG) was utilized to accelerate the convergence. In order to guarantee the stability of the calculation, a time step of $5 \times 10^{-6} \text{ s}$ was chosen.

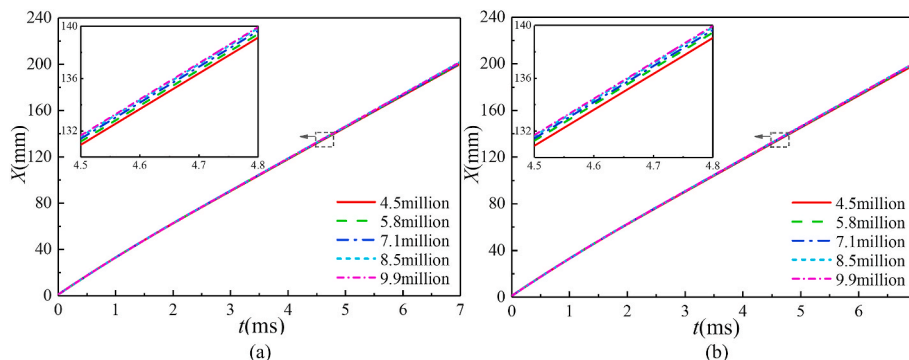


Fig. 5. The vertical displacement of the vehicle with different grid numbers in (a) 0 ice and (b) 1 ice.

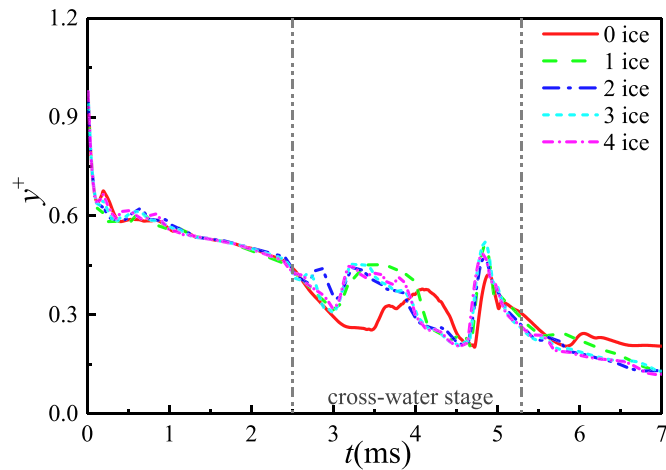


Fig. 6. The maximum value of y^+ value on the vehicle.

3. Validation of the present numerical model

3.1. Accuracy validation

To verify the correctness of the established numerical methodology in high-speed water exit, the same parameters of the vertical water exit and the vehicle, with a diameter of 70 mm, a length of 500 mm, and a

mass of 1.9 kg, as in the experiment done by Wang et al. (2016) are used. A comparison of the experimental and simulated results of the cavity evolution during the water exit is provided in Fig. 3. The cavity is generated by cavitation effects at the head and tail of the vehicle and experiences the process of growth, shedding, and collapse in sequence. There is a good agreement between the experimental and numerical calculation results regarding the shape and size of the water-exit cavity.

Fig. 4 presents the comparison of the velocity of the vehicle. As the vehicle approaches the water surface, its speed continues to decay. Considering experimental measurement errors and other factors, the simulated curve and experimental data have similar magnitudes and variation trends, which verifies that the established numerical methodology can accurately describe the process of vertical water exit of the vehicle. On this basis, a comparative study of the influence mechanisms of no ice versus different quantities of floating ice on the cavity evolution and motion characteristics of an underwater vehicle during the high-speed water exit.

3.2. Grid-independence validation

To eliminate the influence of grid quantity on the calculation results, five different grid densities are established under the premise of ensuring the division rules of overlapping mesh and background mesh. The grid quantities are 4.5 million, 5.8 million, 7.1 million, 8.5 million, and 9.9 million, respectively, in which the first layer of the grid dimensions are 4×10^{-6} m, 2×10^{-6} m, 1×10^{-6} m, 5×10^{-7} m, and 2.5×10^{-7} m, respectively. Based on the numerical methodology

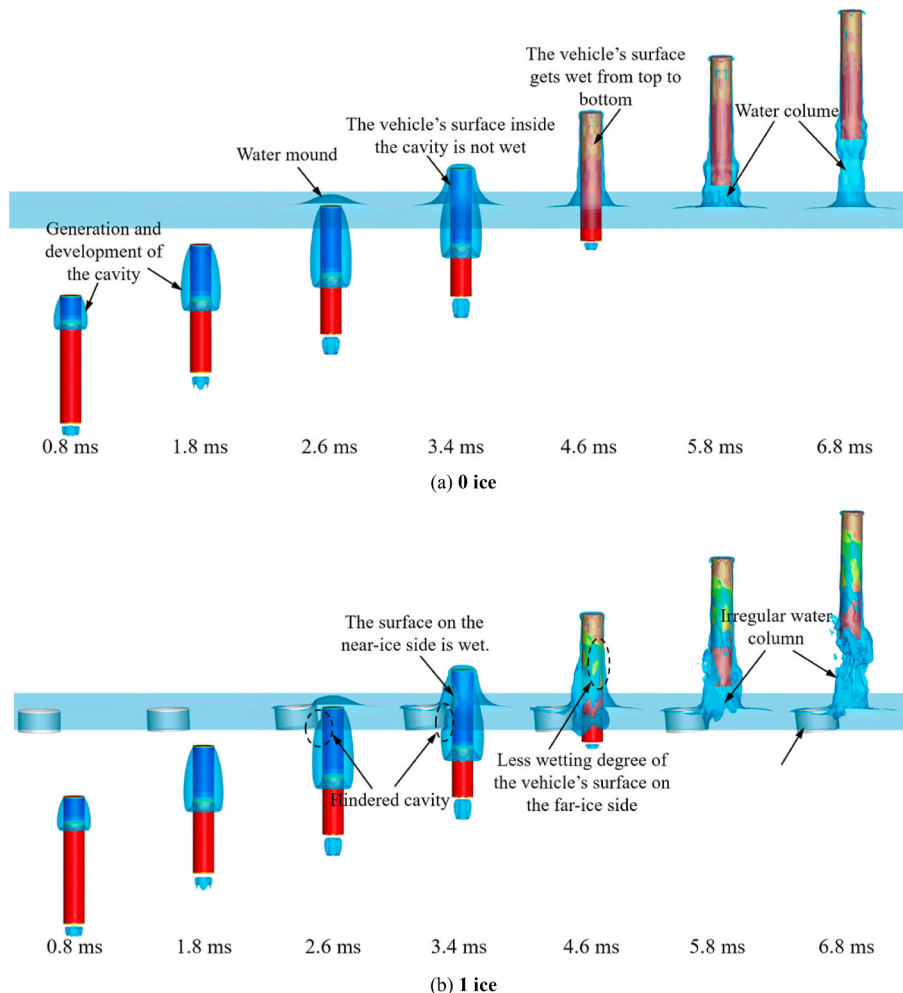


Fig. 7. The water-exit cavity evolution under different quantities of floating ice.

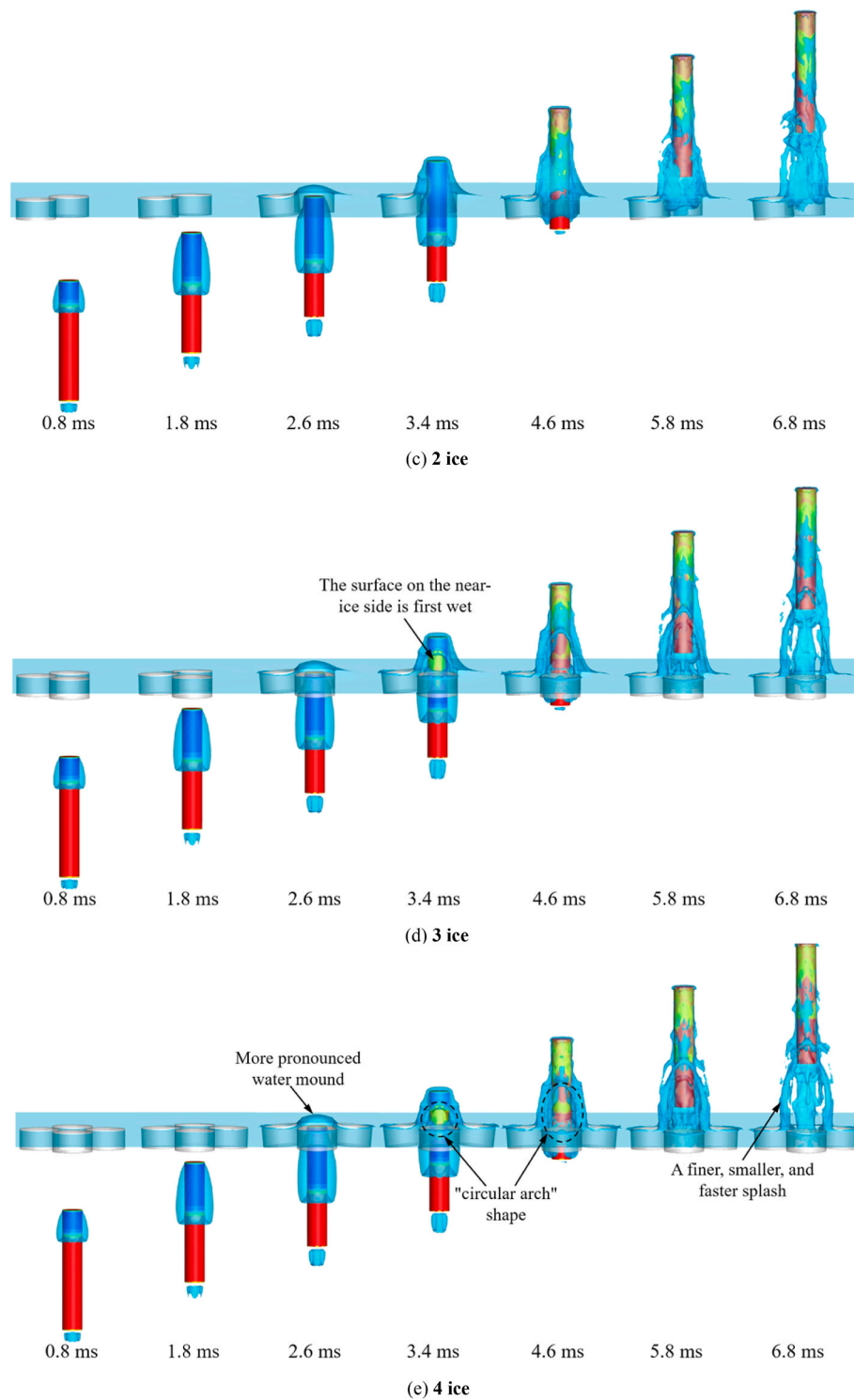


Fig. 7. (continued).

mentioned above, numerical simulations of **0 ice** and **1 ice** are performed to obtain the vertical displacement of the vehicle under various grid densities, as shown in Fig. 5. The vertical displacement of the vehicle in different density grids only shows a slight difference in the cross-water stage, and the variation gradually diminishes as the quantity of the grid increases. Considering the accuracy of the calculation results and the economy of computational resources, a grid number of 7.1 million is chosen for subsequent simulation.

3.3. Validation of y^+

The dimensionless distance y^+ from the wall surface is used to describe the relationship between the grid size and the turbulent structure within the boundary layer, which is defined as:

$$y^+ = (\gamma \rho_m u_\tau) / \mu_m \tag{10}$$

Where y is the vertical distance from the wall, u_τ is the wall friction velocity.

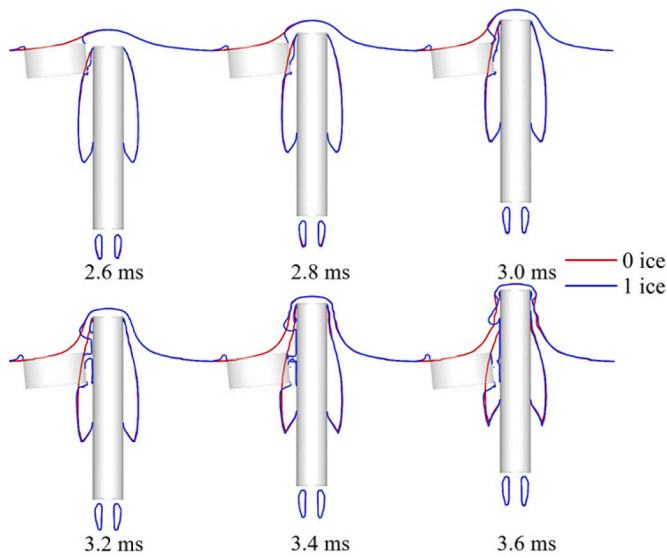


Fig. 8. The influence mechanism of floating ice on the flow pattern of water-exit cavity near the free liquid surface.

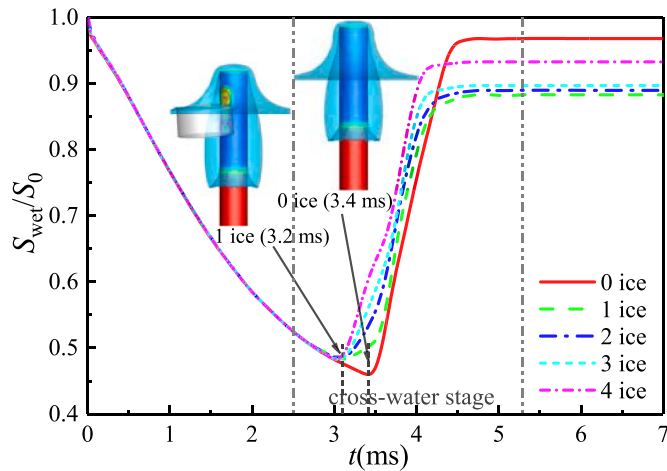


Fig. 9. The wetting degree of the vehicle under different quantities of floating ice.

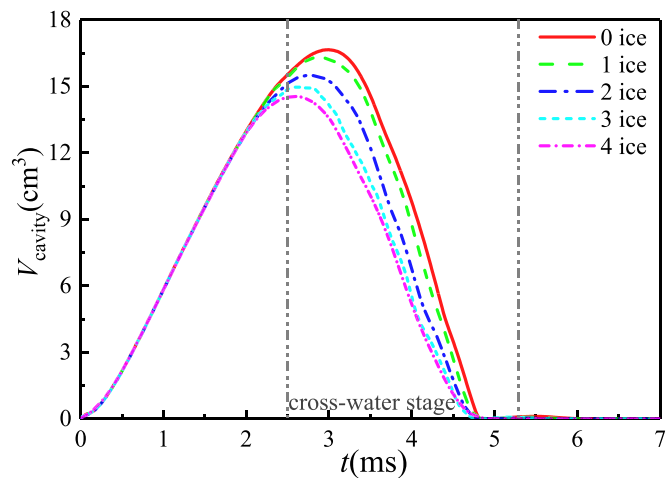


Fig. 10. The volume change of cavity under different quantities of floating ice.

By monitoring the maximum value of y^+ on the surface of the vehicle (Fig. 6) to verify whether it meets the requirement of the SST $k-\omega$ turbulence model. In the initial stage of the motion of the vehicle, the flow field is not entirely stable, and y^+ is relatively high. As cavitation forms and the vehicle speed gradually decreases, y^+ drops steadily. During the cross-water stage, the vehicle undergoes a sudden transition from underwater to air. Due to the significant differences in parameters such as density and viscosity coefficient between water and air, the flow field at this stage is extremely nonlinear, with considerable fluctuations in y^+ . With floating ice, the flow field is more complex, and the y^+ fluctuation is more intense. Since the y^+ in all cases is in the order of 1, the SST $k-\omega$ turbulence model's requirement is satisfied.

4. Results and discussion

4.1. Influence of the quantity of floating ice on the high-speed water exit

4.1.1. Water-exit cavity evolution

Fig. 7 illustrates the evolution of the cavity and free liquid surface during the high-speed water exit through the floating ice gap, considering different quantities of floating ice (0 ice, 1 ice, 2 ice, 3 ice, and 4 ice). The influence of floating ice on the water-exit cavity evolution is primarily investigated during the underwater and cross-water stages, in which the cross-water stage refers to the period starting from the head of the vehicle reaching the hydrostatic level until its tail completely emerges from the water surface.

During the high-speed movement of a submerged vehicle in water, the surrounding water flow is stretched and accelerated to form a high-speed flow. According to the Bernoulli principle, the local pressure drops below the saturated vapor pressure, resulting in cavitation. The fluid flow separates from the head of the vehicle, forming a shoulder-shaped cavity (Fig. 7, 0.8 ms) that gradually increases in length and width as the vehicle rises. The vehicle's head and tail end faces, as well as the portion of the vehicle not covered by the cavity, get wet during the underwater stage (Fig. 7, 0.8–2.6 ms). At this stage, the shape of the cavity under different quantities of floating ice is the same.

Under 0 ice, the water mound phenomenon appears as the vehicle gradually approaches and passes over the hydrostatic level. The fluid near the water surface gains upward velocity due to the compression of the upward-moving vehicle and the cavity. Consequently, the free surface deforms slightly and rises upwards, exhibiting an axisymmetric shape with a gradually decreasing height along the radial direction (Fig. 7a, 2.6 ms). In addition, an obvious re-entrant jet can be observed at the end of the vehicle's shoulder cavity and within the tail cavity. The tail cavity is penetrated by the re-entrant jet and has never come into contact with the end face of the vehicle's tail.

At 3.4 ms, a critical point is reached where the shoulder cavity in 0 ice begins to collapse. As the rising vehicle penetrates the free liquid surface, the cavity near its head starts to shrink from top to bottom under the action of internal and external pressure differences and surface tension. Within a very short period, the cavity collapses completely, with the liquid near the vehicle's head forming a covering water layer on its upper surface (Fig. 7a, 4.6 ms). The surface of the vehicle previously wrapped by the cavity gets wet from top to bottom. Concurrently, the tail cavity also undergoes contraction. By comparing the cavity shape of 4.6 ms under different cases, it can be found that the increase in disturbance caused by more floating ice leads to a higher contraction rate of the tail cavity. The thickness of the water layer gradually becomes thinner under the influence of gravity and aerodynamic forces (Fig. 7a, 5.8 ms). After the vehicle exits the water surface, the upward-moving viscous fluid particles near its tail still possess a certain speed, merging with the water layer flowing into the lower parts of the vehicle and forming a water column at the tail of the vehicle.

The impact of floating ice on the cavity becomes evident since the phenomenon of a water mound. Taking 0 ice and 1 ice as an example for comparative illustration. Fig. 8 depicts how the presence of floating ice

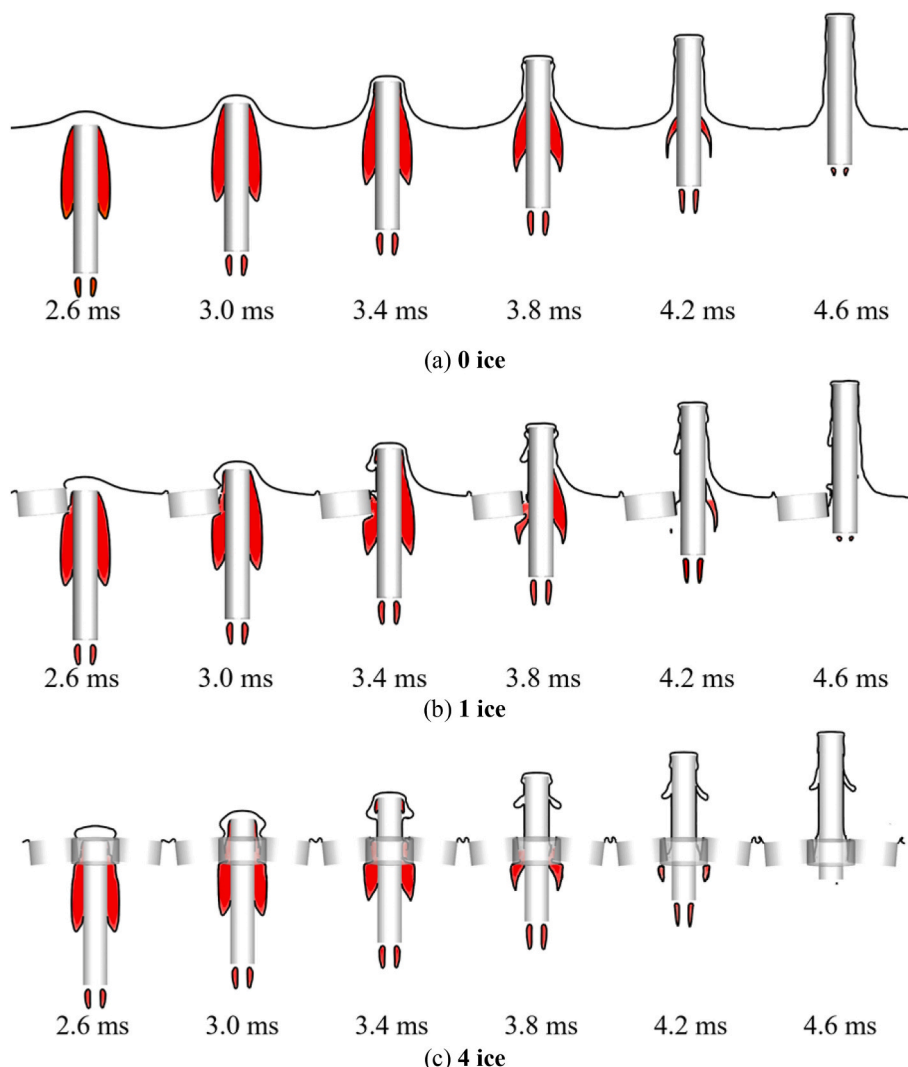


Fig. 11. The distribution of vapor in the cavity under different quantities of floating ice.

affects the flow pattern of the water-exit cavity near the free liquid surface (2.6–3.6 ms). Ice, being solid with higher inertia than water, hinders the development of the water-exit cavity as the vehicle moves upward. Consequently, the previously axisymmetric cavity and water mound become distorted. The cavity on the near-ice side bends and moves closer to the wall, accelerating its contraction and collapse, which will also lead to earlier contact of the vehicle with the free liquid surface, resulting in premature wetting (Fig. 8, 3.2 ms). Additionally, the free surface near the head of the vehicle on the far-ice side appears slightly wrinkled instead of smooth (Fig. 8, 3.4–3.6 ms), although the moment when the cavity begins to contract remains the same as in the absence of ice (3.6 ms). In situations where four ice floes surround the water-exit point, the movement area of fluid above the vehicle's head is restricted to the vicinity of the water-exit point due to the obstruction caused by floating ice, resulting in a more pronounced water mound (Fig. 7e, 2.6 ms).

Fig. 9 illustrates the wetting degree of the vehicle under different quantities of floating ice. Initially, the vehicle is completely wet, and its motion starts from static. The wetting degree gradually declines steadily with the gradual expansion of the cavity. In 0 ice, the lowest wetting degree occurs just before the cavity collapses (Figs. 8 and 9, 3.4 ms). After the vehicle leaves the water surface, a uniform water layer almost completely covers its surface (Fig. 7a and 5.8–6.8 ms), meaning that the wetting degree is the highest under 0 ice.

The impact of floating ice on the wetting of the vehicle becomes apparent during the cross-water stage. Floating ice causes the free liquid surface near its side to develop into a "circular arch" shape, resulting in the bending of the cavity on the near-ice side and thus accelerated contraction and collapse (Fig. 7b–e, 3.4–4.6 ms). The fluid in the middle of the "circular arch" free liquid surface rapidly approaches the wall, leading to earlier wetting of the vehicle (Figs. 8 and 9, 3.2 ms), and the growth rate of its wetting degree increases with the quantity of floating ice.

The presence of floating ice alters the distribution area of the water layer on the vehicle's surface. The fluid in the middle of the "circular arch" free liquid surface is depressed inward and thinner, closer to the vehicle, while the fluid on both sides expands outward and thicker, resulting in the water layer no longer being uniform and unable to completely cover the vehicle, thus reducing the wetting degree of the vehicle's surface on the far-ice side (Fig. 7b–d, 4.6–6.8 ms). As shown in Fig. 9, after the vehicle leaves the water surface, the wetting degree is the lowest in 1 ice and higher in 4 ice, which indicates that the wetting degree progressively increases with the quantity of floating ice, as four evenly distributed ice floes surround the water-exit point in 4 ice. Wetting occurs first on the near-ice side of the vehicle, meaning that the far-ice surface is no longer present, resulting in a limited reduction in wetting (Fig. 7e, 4.6–6.8 ms).

Due to the influence of floating ice near the water-exit point, the

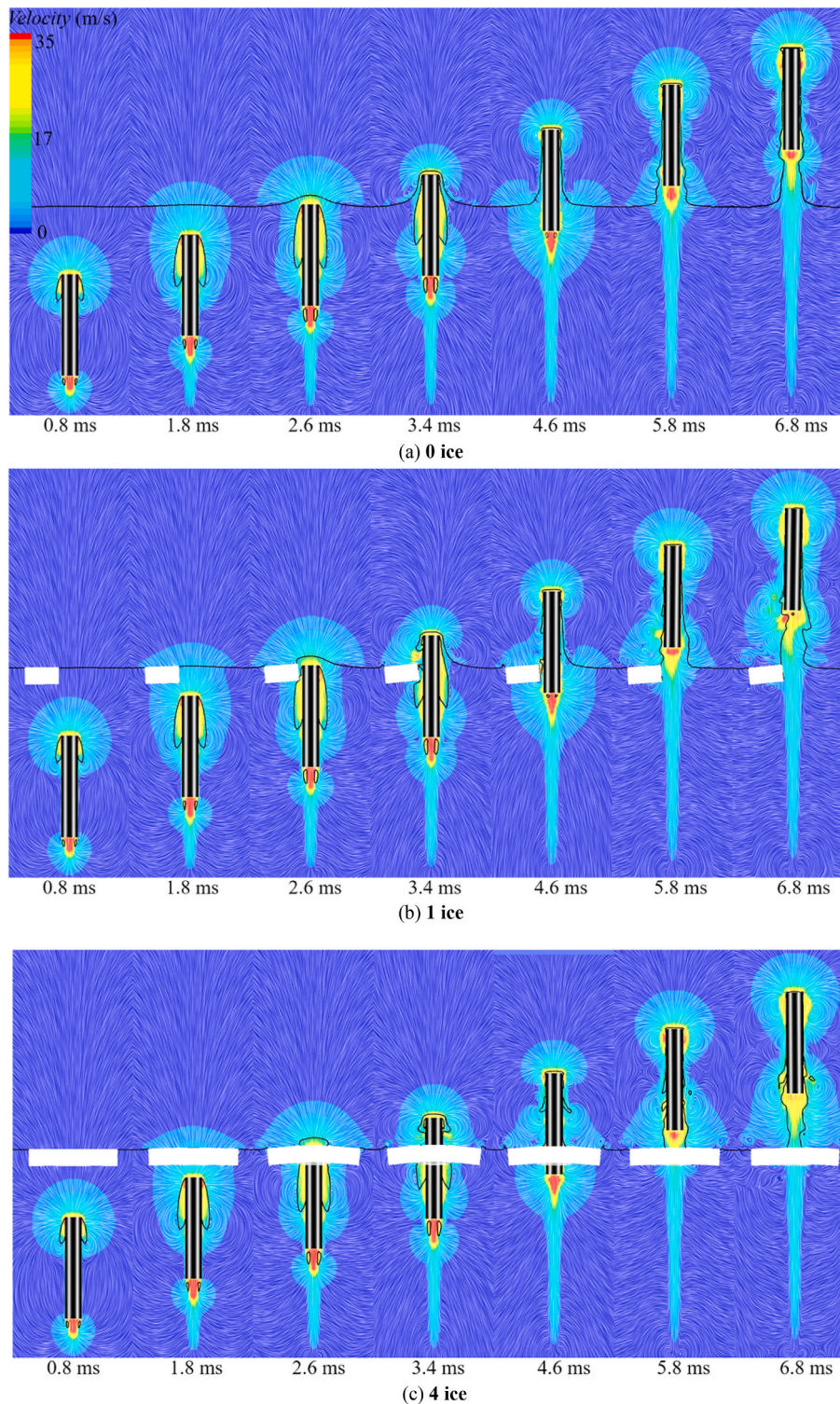


Fig. 12. The distribution of the velocity field on the xoy symmetry plane under different quantities of floating ice.

shape of the water column after the vehicle exits the water varies greatly from that without ice and is related to the distribution of floating ice. The fluid particles on the near-ice side behind the vehicle encounter hindrance and cannot directly emerge from the water-exit point. During the interaction with the floating ice, the fluid on both sides expands outward, resulting in an irregular water column in 1–3 ice, with a thicker water column on the far-ice side. In situations where two or more ice floes surround the water-exit point, part of the liquid can only emerge from the gaps between the ice floes, showing a finer, smaller,

and faster splash (Fig. 7e, 6.8 ms), instead of a regular water column (Fig. 7a, 6.8 ms).

The cavity of the non-ventilated submarine-launched vehicle during underwater movement is generated by the cavitation effect and is filled with vapor. Therefore, the vapor volume corresponds to the volume of the water-exit cavity. Fig. 10 illustrates the cavity volume change of the vehicle passing through the ice floe gap during the high-speed water exit. During the underwater stage, the volume of the water-exit cavity increases steadily, which holds same for all cases. However, as the

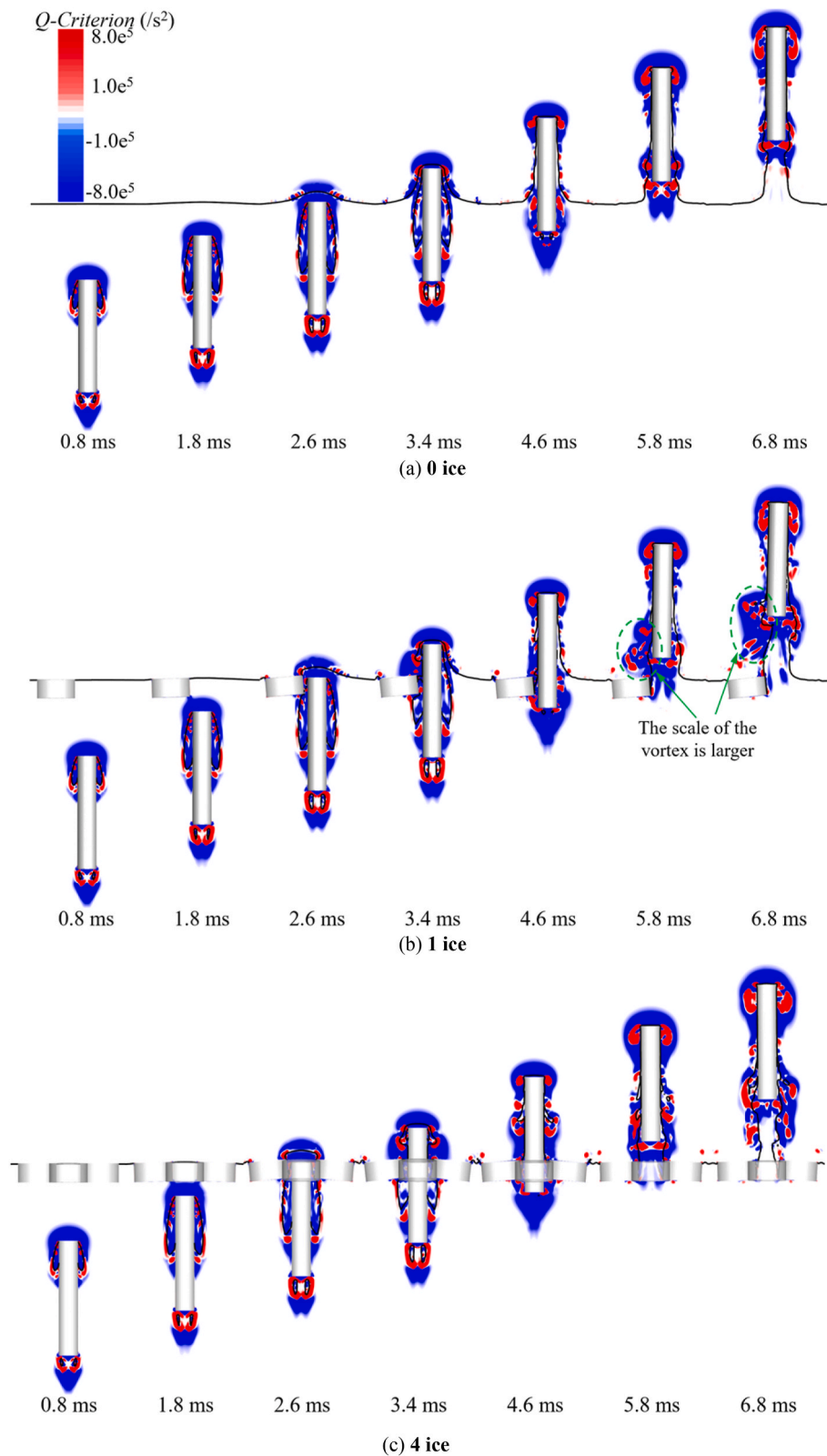


Fig. 13. The distribution of Q values on the xoy symmetry plane under different quantities of floating ice.

vehicle gradually approaches the ice floes of the free surface, the volume of the cavity begins to vary. Due to the obstruction of the ice, the cavity on the near-ice side is bent, and the volume increase rate decreases, with the magnitude of the decrease increasing with the quantity of floating ice. During the cross-water stage, the cavity volume reaches its peak

before the vehicle penetrates the free surface. Subsequently, due to the effect of internal and external pressure differences and surface tension, the cavity cannot continue to maintain, leading to contraction and collapse. Consequently, there is a rapid reduction in vapor content. Notably, the peak value of cavity volume is the largest in 0 ice, while the

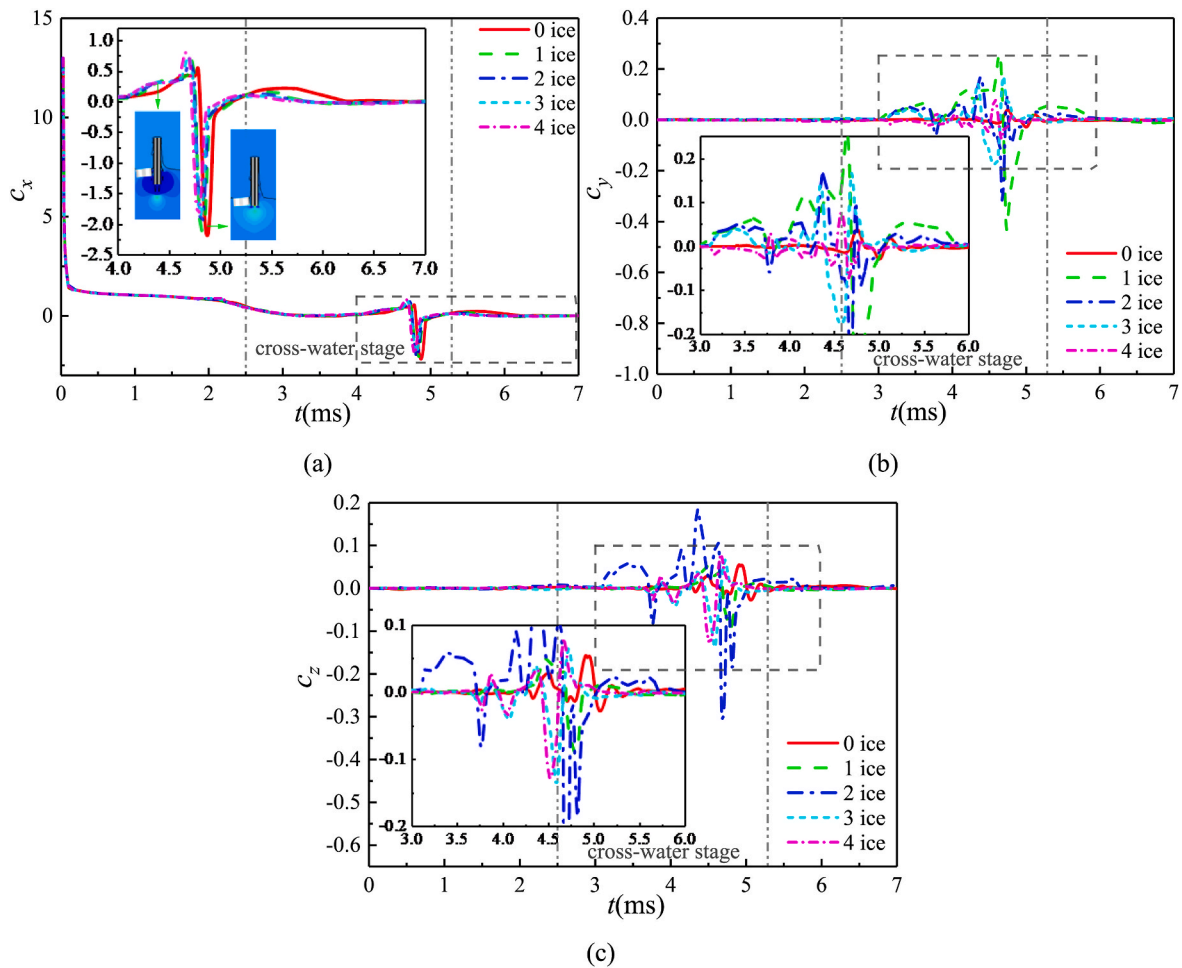


Fig. 14. The force coefficients of the vehicle under different quantities of floating ice: (a) in the x-direction; (b) in the y-direction; (c) in the z-direction.

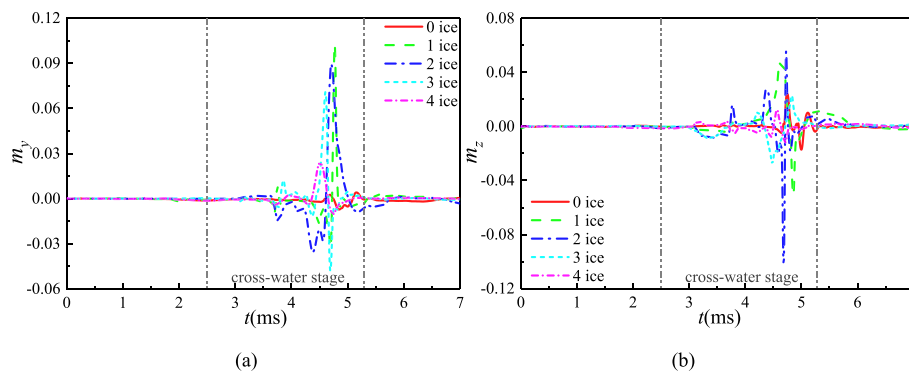


Fig. 15. The horizontal moment coefficients of the vehicle under different quantities of floating ice: (a) in the y-direction; (b) in the z-direction.

smallest in 4 ice. Additionally, the decay moment occurs earlier with the quantity of floating ice, indicating that the influence degree of the volume of the water-exit cavity increases with the quantity of floating ice.

By comparing 0 ice and the *xoy* symmetrical plane with the presence of floating ice (1 ice, 4 ice), the influence process of floating ice on vapor during the cross-water stage is explored, as illustrated in Fig. 11. Floating ice impedes the development of the cavity near its side, causing the cavity to wrinkle and bend. In situations where two or more ice floes, a certain degree of compression of vapor occurs inside the cavity before the cavity collapses (Fig. 11b–c, 2.6–3.0 ms). At 3.4 ms, the excessively bent cavity collapses, and the internal balance of the cavity has been broken. A large amount of vapor on the near-ice side liquefies into

water, resulting in rapid decay of vapor content (Fig. 11b, 3.4–4.2 ms). In 4 ice, due to four evenly distributed ice floes surrounding the water-exit point, the vapor inside the cavity decays more rapidly.

4.1.2. Distribution of the velocity field and dynamic characteristics of unsteady vortex structures

The distribution of the velocity field on the *xoy* symmetry plane under different quantities of floating ice is provided in Fig. 12, which describes the streamline distribution within the exhibited region using line integral convolution (LIC). During the underwater stage and the initial cross-water stage, a high-speed zone appears near the flow separation at the vehicle’s head and the tail cavity (Fig. 12, 0.8–2.6 ms).

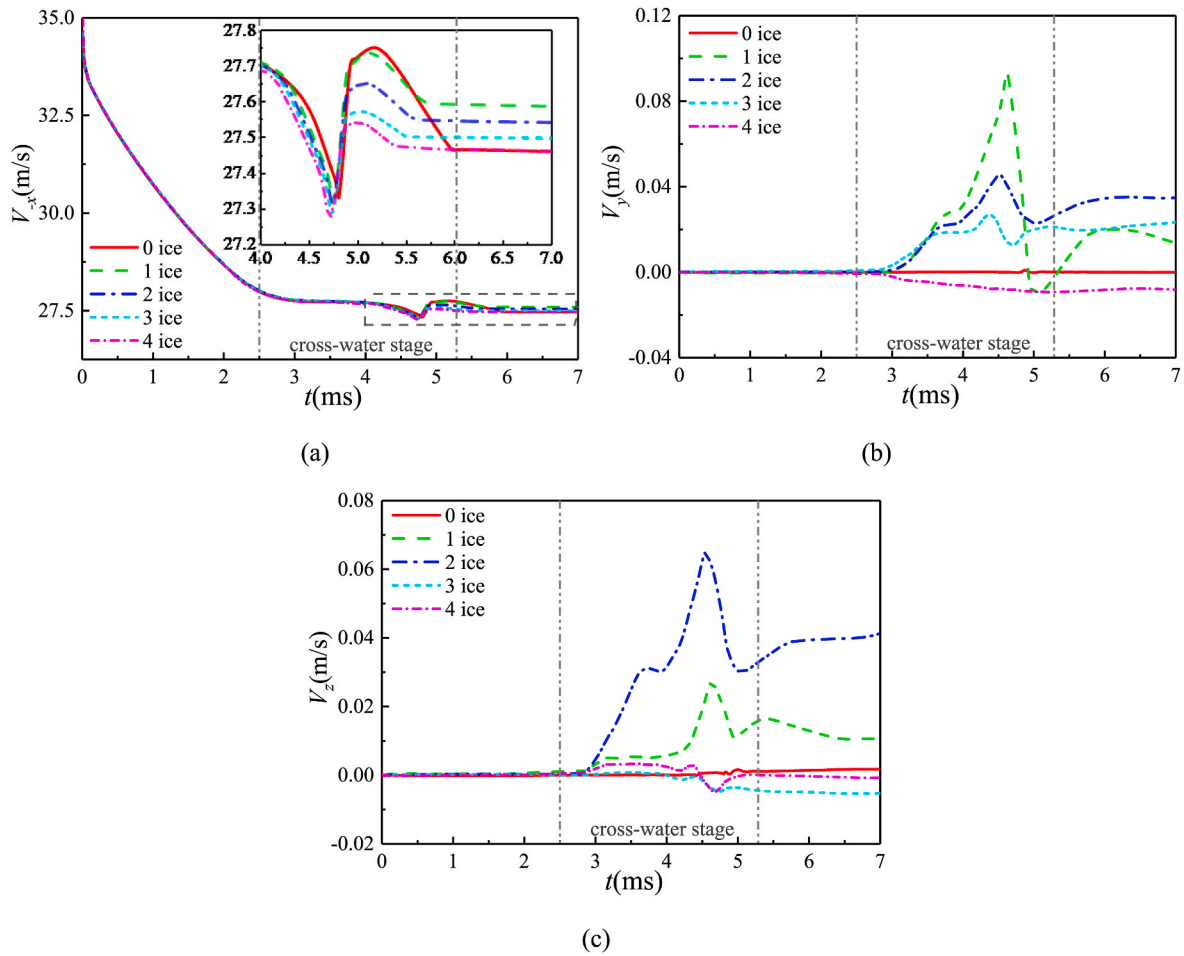


Fig. 16. The velocity variation of the vehicle under different quantities of floating ice: (a) in the x-direction; (b) in the y-direction; (c) in the z-direction.

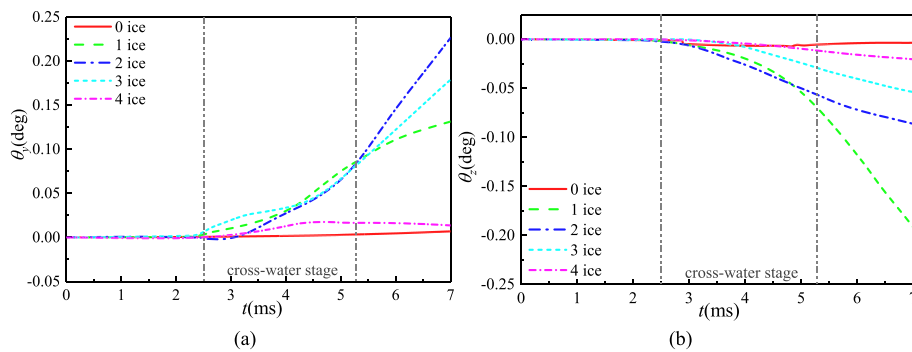


Fig. 17. The attitude angle of the vehicle under different quantities of floating ice: (a) around the y-axis; (b) around the z-axis.

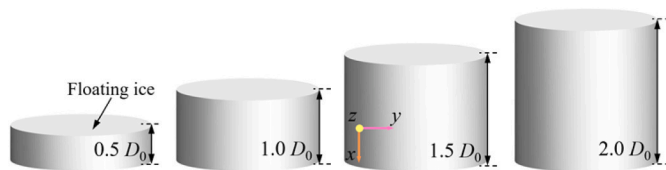


Fig. 18. Schematic diagram of floating ice with different thicknesses (front view).

The rear end of the shoulder cavity exhibits a re-entrant jet with vortex characteristics. This is because the shoulder cavity is completely generated by cavitation effects, and the pressure inside the cavity is saturated vapor pressure. Owing to the pressure difference between the inside and outside of the cavity, the external fluid has a tendency to flow into the cavity. Additionally, the vehicle continues to move upward, causing the viscous external fluid to converge into the low-pressure region in the middle of the shoulder cavity, forming a vortex.

In 0 ice, after the head of the vehicle emerges from the water, the covering water layer near the wall of the vehicle moves downward at a relatively low velocity, intersecting with the wake that has a higher velocity (Fig. 12a, 5.8–6.8 ms). In the later cross-water stage, a high-velocity gradient appears near the vehicle's head (Fig. 12, 6.8 ms),

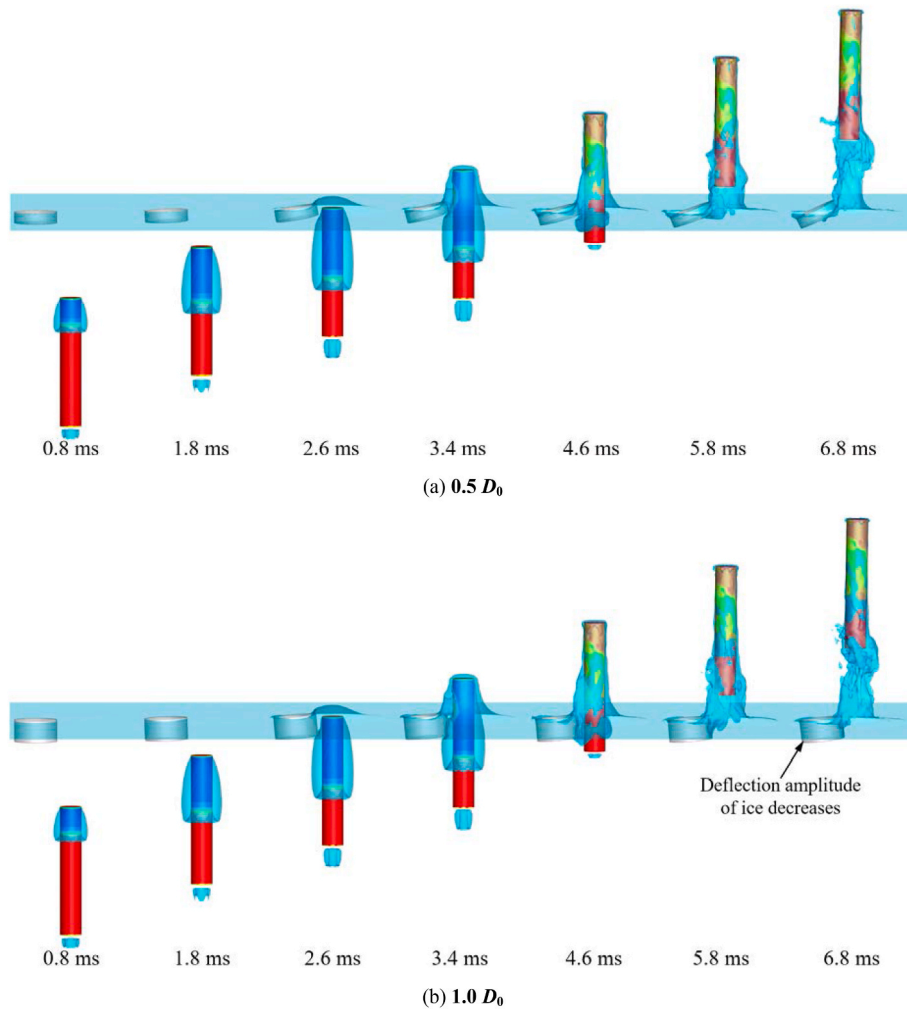


Fig. 19. The water-exit cavity evolution under different thicknesses of floating ice.

which can be attributed to two reasons. Firstly, the medium in front of the vehicle's head is air, which has a significantly lower density and viscosity than water. Therefore, even with small perturbations, it can achieve high velocity, and the high-speed flowing air separates from the edge of the end face. Secondly, the liquid carried by the end face of the vehicle's head is squeezed by the air and splashes downward in the form of water droplets at the edge of the head, which is more evident in the three-dimensional cavity diagram (Fig. 7, 6.8 ms). In the absence of floating ice, the velocity gradient and streamline distribution are basically symmetrical around the vehicle axis.

Apart from altering the form of the cavity, the floating ice close to the water-exit point significantly disrupts the velocity flow field's distribution. On the near-ice side, due to the obstructive effect of the floating ice, the free liquid surface develops into a "circular arch" shape, instead of a uniform covering layer. The cavity on the near-ice side becomes bent and deformed, leading to earlier contraction and collapse. A wide range of high-speed zones appears on the near-ice side as a result of the high-speed vapor inside the cavity leaking out of the gap between the floating ice and the vehicle (Fig. 12b, 3.4–6.8 ms). In 1 ice, due to the presence of ice on only one side, the distribution of velocity flow lines is no longer regular. The mechanism of disturbance of the velocity field by a single piece of floating ice in 4 ice is similar to that in 1 ice, but due to the uniform distribution of four ice floes, the distribution of high-speed zones and streamline of the whole flow field is relatively symmetrical.

The generation, development, coupling, motion, and separation of

vortex structures exhibit strong unsteadiness. Vortices organize fluid flow and promote the accumulation of kinetic energy during fluid motion, playing an important role in the generation and maintenance of turbulence. The Q criterion based on the Eulerian method is used to describe the vortex structure:

$$\begin{cases} Q = \frac{1}{2}(\Omega^2 - S^2) \\ \Omega = \frac{1}{2}\left(\frac{\partial u_i}{\partial x_j} - \frac{\partial u_j}{\partial x_i}\right) \\ S = \frac{1}{2}\left(\frac{\partial u_i}{\partial x_j} + \frac{\partial u_j}{\partial x_i}\right) \end{cases} \quad (11)$$

Where Ω is the rotation tensor, S denotes the shear strain rate tensor, $Q > 0$ represents the vortex structure, $Q < 0$ means the shear deformation effect.

Fig. 13 depicts the Q -value distribution on the xoy plane, combined with the streamline distribution in Fig. 12 to analyze the dynamic characteristics of the vortex structure. Before the vehicle penetrates the free liquid surface (Fig. 13a, 0.8–2.6 ms), vortices below the water surface are attached to the surface of the cavity, accompanied by the development of the cavity. The vortex structures at the rear end of the vehicle become stronger and larger as the cavity develops. The large negative Q values at the rear end of the cavity and the tail cavity indicate the existence of strong shear deformation effects in this region, which is

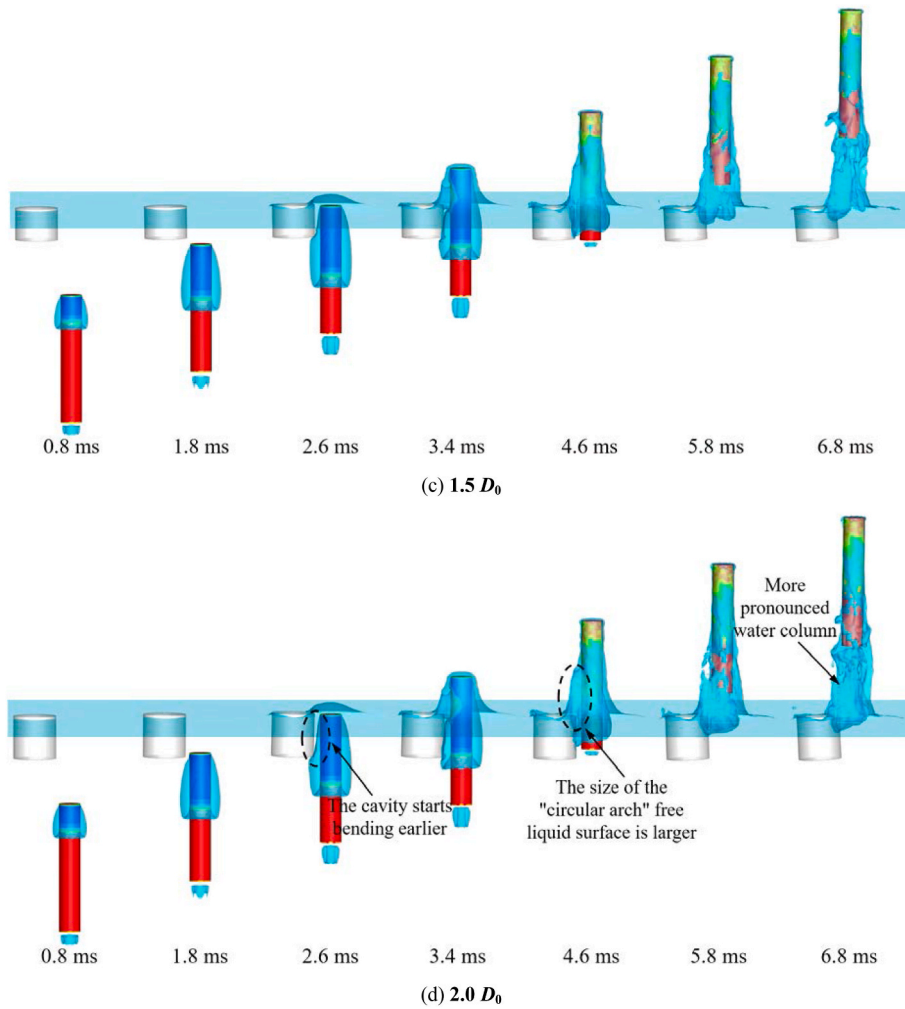


Fig. 19. (continued).

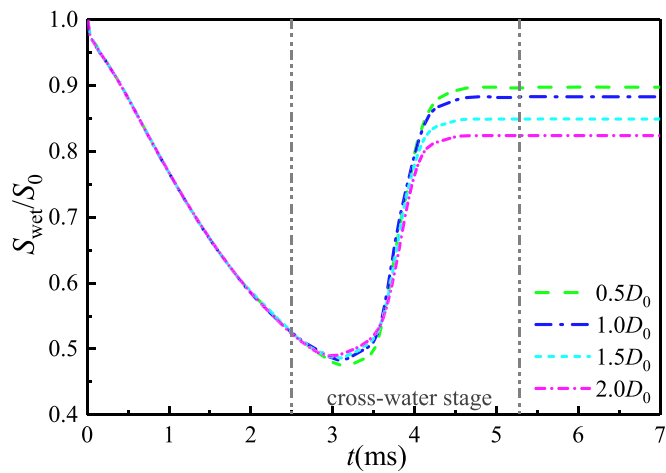


Fig. 20. The wetting degree of the vehicle under different thicknesses of floating ice.

consistent with the streamline convergence area. During the underwater stage, the scale of the vortex remains relatively constant, but the number gradually increases, with alternating positive and negative Q values. Vortex and shear deformation jointly dominate the development of the cavity. In the initial cross-water stage, there are a few vortex structures

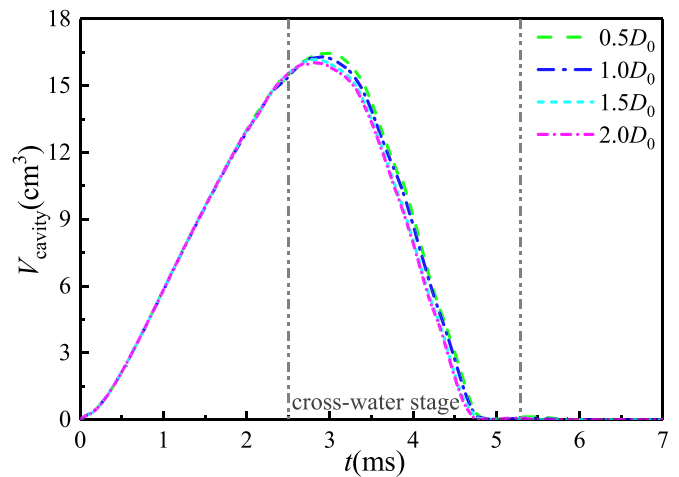


Fig. 21. The volume change of cavity under different thicknesses of floating ice.

around the top of the water mound (Fig. 13a, 2.6 ms), but the shear deformation effect dominates and coincides with the region where the streamline originates. It can be seen that the shear deformation effect mainly occurs in the streamline convergence and starting area. The vortex structure mainly develops in the later cross-water stage, and the

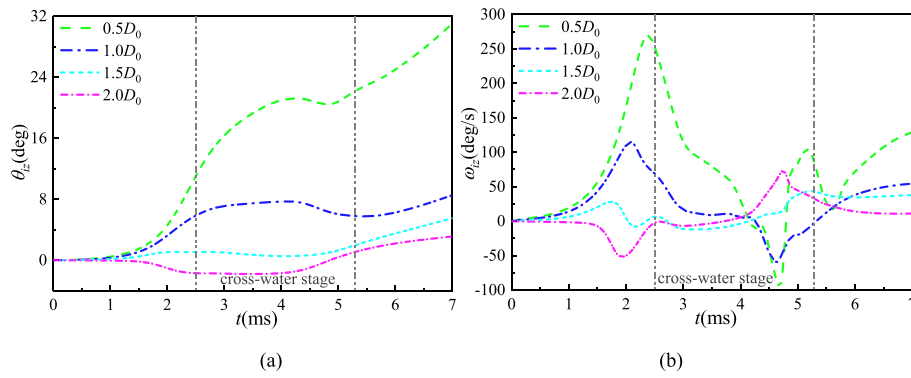


Fig. 22. The deflection attitude change around the z-axis of floating ice with different thicknesses: (a) deflection angle; (b) deflection angular velocity.

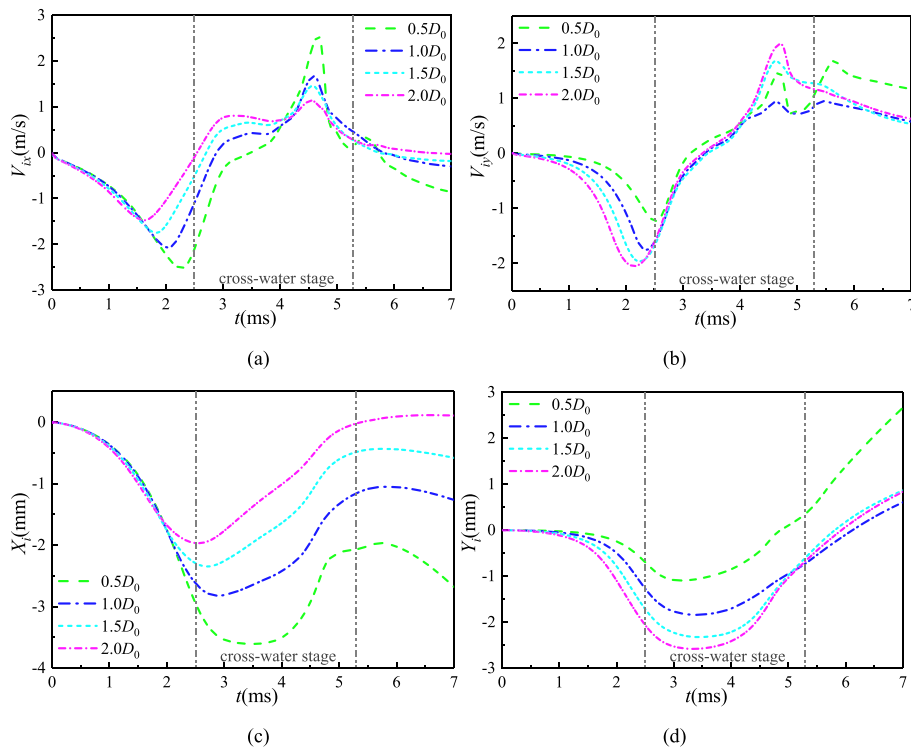


Fig. 23. The velocity and displacement of floating ice with different thicknesses: (a) vertical velocity; (b) horizontal velocity; (c) vertical displacement; (d) horizontal displacement.

scale of the vortex structures at the front section of the head increases significantly as the vehicle rises. The convergence and accumulation of the upward-moving wake flow at the rear end of the vehicle and the downward-moving water layer provide energy for the motion and development of the vortices in the vicinity. Consequently, the number and intensity of the vortices gradually increase (Fig. 13a, 5.8–6.8 ms).

The presence of ice significantly changes the distribution and motion characteristics of the vortex structures. Specifically, the shear deformation effect at the top of the "circular arch" free liquid surface on the near-ice side is more pronounced (Fig. 13, 3.4 ms). Due to the obstruction of ice, the cavity shape becomes bent and deformed, causing earlier contraction and collapse, and high-speed vapor leaks out from the gap between the ice and the vehicle, which provides energy for the motion and development of the vortices in the vicinity. The vortex on the near-ice side has a larger area, as well as a higher number and intensity compared to 0 ice. Besides, a large number of vortices above the ice continue to stretch and expand while moving outward. In 4 ice, due to the uniformly distributed ice floes around the water-exit point, vapor

overflows from all sides, hence the area of vortex diffusion on the near-ice side is slightly smaller than that of 1 ice. Due to the obstruction of ice floes, part of the fluid moving behind the vehicle forms a backflow under the ice. As a result, there are also a small number of vortices on the side near the vehicle under the floating ice.

4.1.3. Hydrodynamics and motion characteristics of the vehicle

In order to further investigate the influence of different quantities of floating ice on the hydrodynamics and motion characteristics of the submarine-launched vehicle during the high-speed water exit, the force coefficients and moment coefficients are both dimensionless, with expressions as follows:

$$c_i = \frac{F_i}{0.5\rho_1 v^2 S} \quad (12)$$

$$m_i = \frac{M_i}{0.5\rho_1 v^2 SL} \quad (13)$$

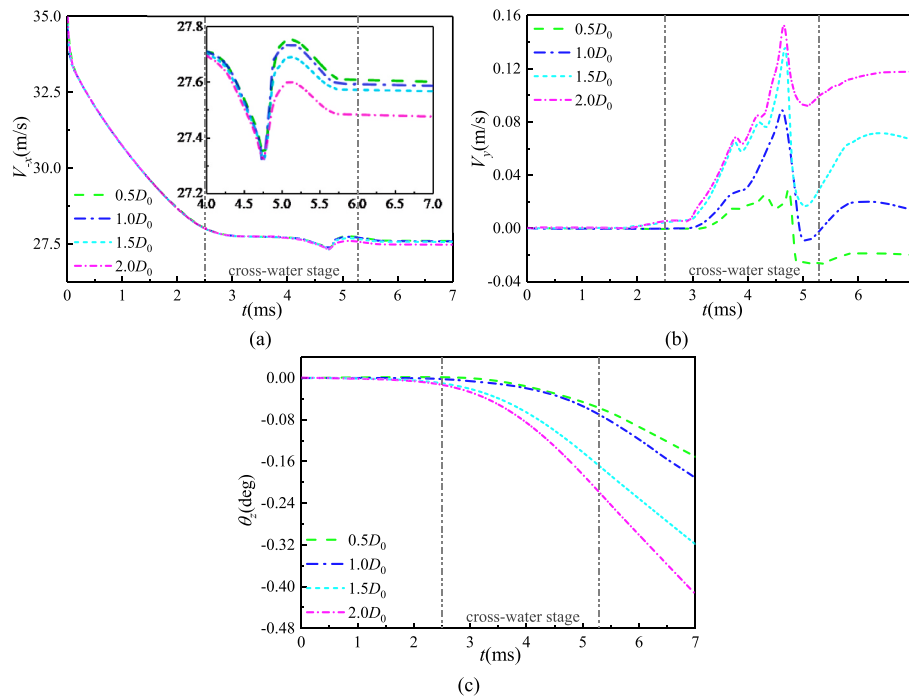


Fig. 24. The motion characteristics of the vehicle under different thicknesses of floating ice: (a) vertical velocity; (b) horizontal velocity; (c) pitch angle change around the z-axis.

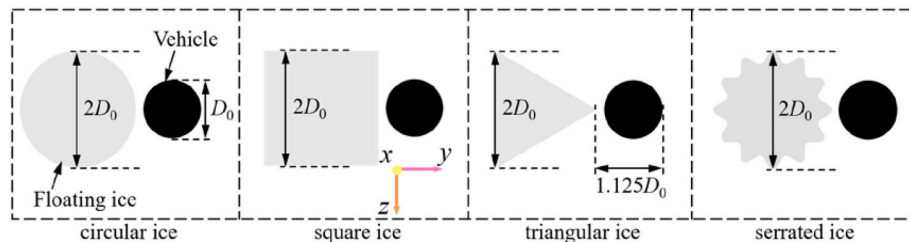


Fig. 25. Distribution of the vehicle and floating ice with different shapes at the initial moment (top view).

Where F_i and M_i are the force and moment acting on the vehicle in the i direction, respectively. S denotes the characteristic area of the vehicle, $S = \pi D_0^2/4$. v is the moving speed of the vehicle.

Fig. 14a illustrates the force coefficients in the x direction of the vehicle under different quantities of floating ice. At the initial moment of the vehicle's motion, the stationary fluid particles around its head gain potential energy and begin to move. As a result of force interactions, significant resistance is exerted back onto the vehicle. During the vehicle's upward movement, the drag force in the vertical direction steadily decays with the formation and development of the cavity.

The fluctuation of the vertical force coefficient curve occurs during the later cross-water stage. The majority of the vehicle's surface is exposed to the atmospheric environment, and since the tail cavity has not yet collapsed, the area near the tail of the vehicle remains close to the saturated steam pressure. During this stage, the vehicle is not only subjected to gravity and additional mass force but also to the pressure difference between the upper and lower parts, resulting in a slight increase in the downward resultant force. Subsequently, the resultant force reaches a short-lived reverse extreme value, accelerating the vehicle, which is caused by the local high pressure generated during the collapse of the tail cavity. After the vehicle leaves the water surface, it is only subjected to gravity and additional mass force. As the water layer flows downward, the force coefficient gradually decreases and tends to be stable. Furthermore, in cases with floating ice, the cavity collapses

earlier compared to 0 ice due to the disturbance of floating ice, causing the aforementioned processes to occur earlier as well.

Figs. 14b, 14c, 15a and 15b present the curves depicting the horizontal force coefficients and moment coefficients of the vehicle, respectively. During the cross-water stage, the cavity collapses due to the internal and external pressure difference and surface tension, oscillations occur in the horizontal force coefficients and moment coefficients, which gradually attenuate as the vehicle leaves the water surface. The amplitude of the curve fluctuation in the presence of ice is much more severe than that in 0 ice. Moreover, in situations where ice floes are asymmetrically distributed (1 ice, 2 ice, 3 ice), in the direction of the ice, the hydrodynamic force and moment acting on the vehicle are stronger, with more drastic changes and longer fluctuation durations. This phenomenon arises from the uneven distribution of ice, which induces asymmetric alterations in the free liquid surface, affects the evolution of the cavity, changes the symmetry of the distribution of the water layer on the vehicle and the flow field structure around the vehicle, causing more severe fluctuations in the hydrodynamic force.

Fig. 16 shows the velocity variation of the vehicle under different quantities of floating ice. Fig. 17 presents the attitude angle changes during the water exit of the vehicle. During the later cross-water stage, the saturated vapor pressure only exists near the tail of the vehicle. Due to the pressure difference caused by the atmospheric pressure near the upper of the vehicle, its speed reduction rate increases. As the speed of the tail cavity collapse increases with the quantity of floating ice, the

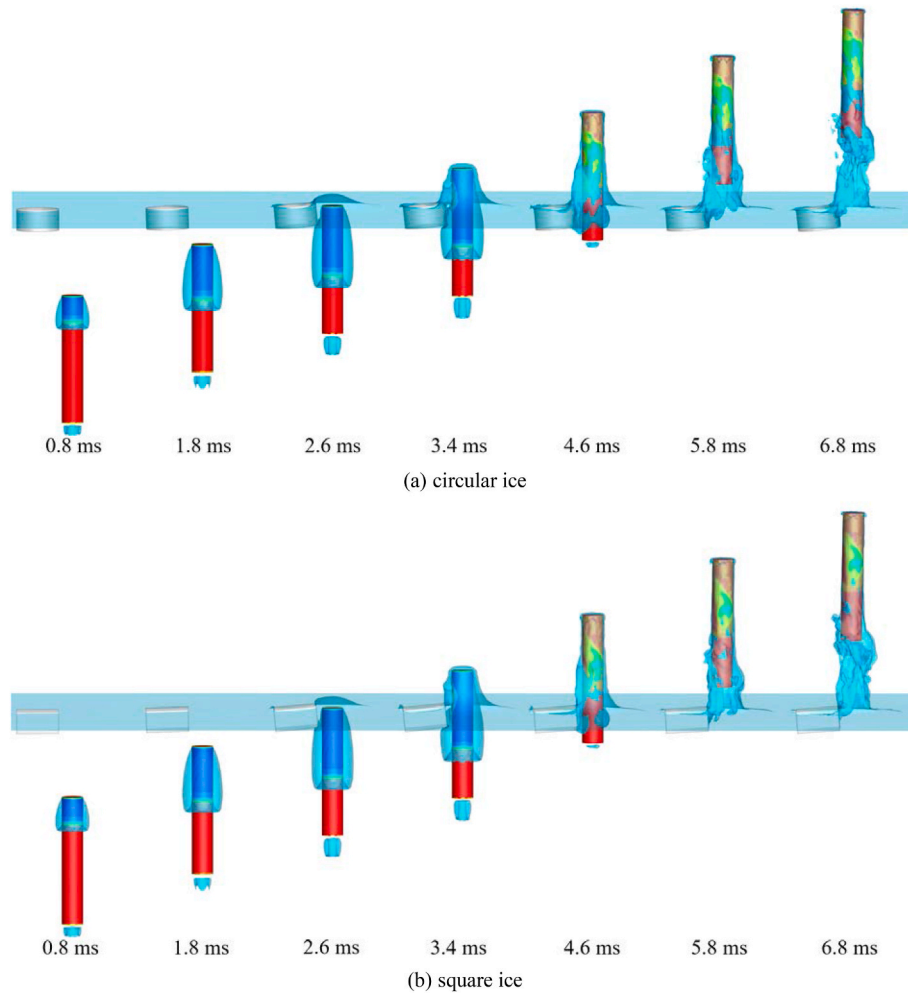


Fig. 26. The water-exit cavity evolution under different shapes of floating ice (front view).

acceleration time of the vehicle in **4 ice** is the shortest, hence it exhibits a different speed compared to **1 ice**. Once the vehicle separates from the water surface, due to the viscosity of the water, the viscous force caused by the attached water is the main source of the fluid resistance of the vehicle. Since the vehicle of **0 ice** carries more water, it experiences the highest degree of speed attenuation. Consequently, in situations where a small amount of floating ice exists around the water-exit point (**1ice**, **2ice**, **3ice**), the vertical velocity of the vehicle after leaving the water surface is slightly higher than that of **0 ice**. During the underwater stage, the vehicle remains unaffected by the floating ice, resulting in stable velocity and attitude angles in the horizontal direction. The variations between different cases become increasingly evident during the cross-water stage. In **4 ice**, owing to the floating ice being symmetrically distributed, the influence on the attitude angle of the vehicle is not significant. However, due to the asymmetrically distributed ice floes (**1ice**, **2ice**, **3ice**) around the water-exit point, the horizontal velocity of the vehicle is greatly disturbed, leading to greater deviations in both horizontal velocity and attitude angle as a result of the floating ice.

4.2. Influence of the thickness of floating ice on the high-speed water exit

To investigate the influence of the varying thicknesses of floating ice on the water-exit cavity and motion characteristics of the vehicle, based on the analysis of the circular floating ice of **1 ice** in the above chapters, keeping the shape and diameter of the floating ice, as well as the initial radial gap between the ice and the edge of the vehicle constant.

Additional cases with ice thicknesses of $0.5 D_0$, $1.5 D_0$, and $2.0 D_0$ are established (Fig. 18), respectively.

4.2.1. Water-exit cavity evolution

The three-dimensional cavity evolution corresponding to cases with ice thicknesses of $0.5 D_0$, $1.0 D_0$, $1.5 D_0$, and $2.0 D_0$ is presented in Fig. 19. Besides, Figs. 20 and 21 reflect the wetting degree of the vehicle and the volume change of cavity under different thicknesses of floating ice, respectively.

By comparing Figs. 19a and 7a, it is evident that even if the ice floe is relatively thin, it still has a significant impact on the cavity evolution during high-speed water exit. The influence follows a similar pattern as discussed in Section 4.1.1 and will not be reiterated. In cases with different thicknesses, the cavity begins to show variations after 1.8 ms. During the underwater stage, as the ice thickness increases, the distance between the cavity and the ice wall decreases, and the cavity starts bending earlier (Fig. 19, 2.6 ms), leading to premature wetting of the upper surface of the vehicle.

During the cross-water stage, the hindering effect on the cavity and free liquid surface development becomes stronger with thicker ice, leading to an extended action time. Concurrently, the size of the "circular arch" free liquid surface in $2.0 D_0$ is much larger than that of $0.5 D_0$ (Fig. 19, 4.6 ms). After the vehicle completely emerges from the water, the degree of wetting on its surface decreases with increasing ice thickness (Fig. 20). This is because thicker ice floes have a stronger destructive effect on the covering water layer, and the larger "circular

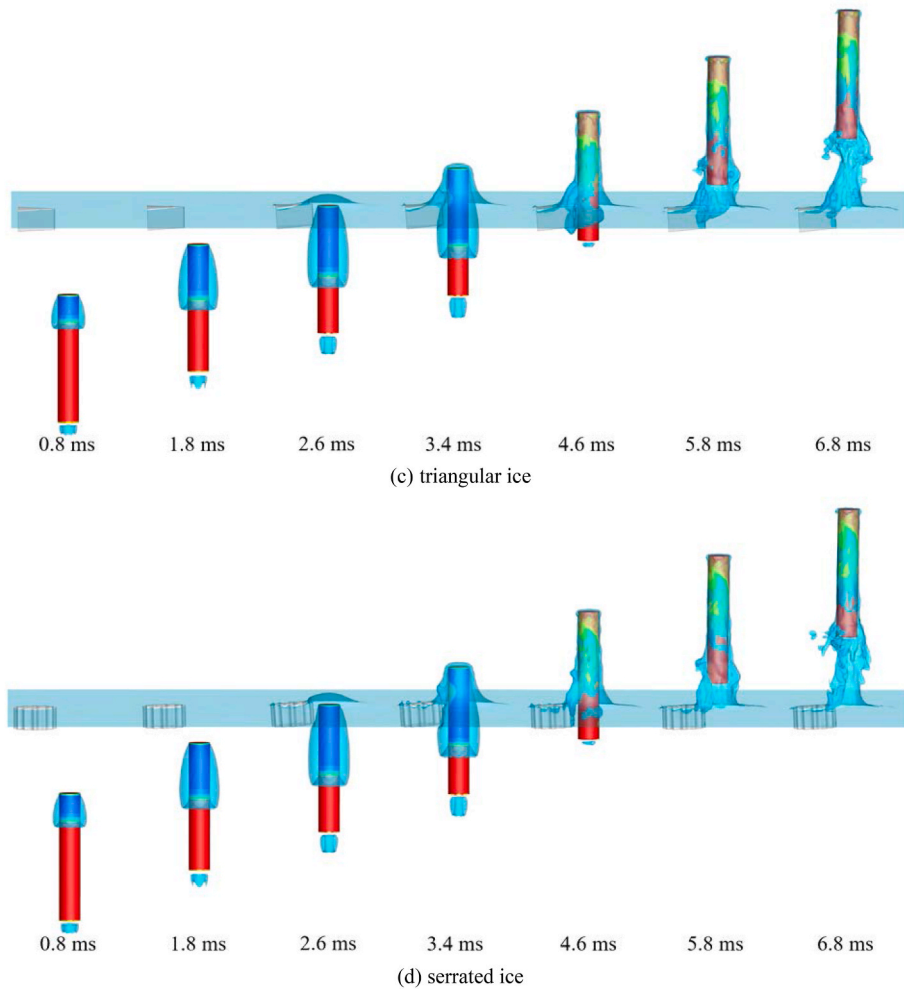


Fig. 26. (continued).

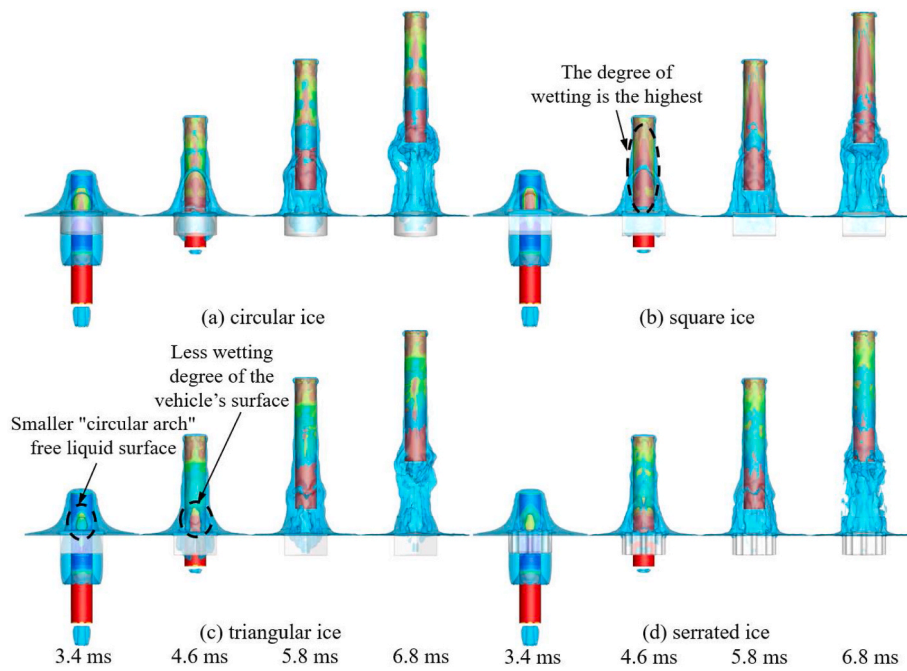


Fig. 27. The water-exit cavity evolution under different shapes of floating ice (near-ice side view).

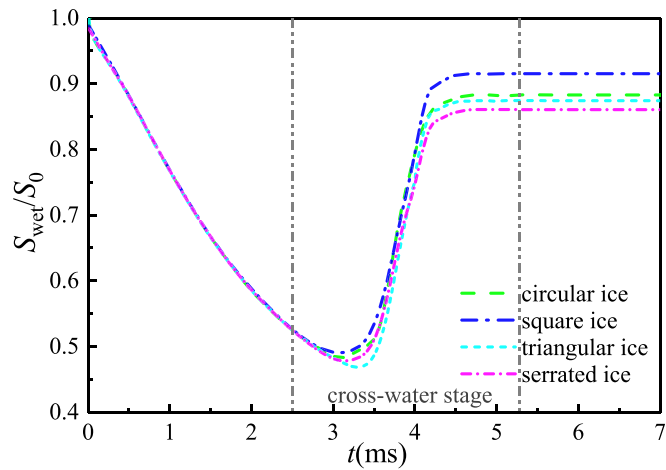


Fig. 28. The wetting degree of the vehicle under different shapes of floating ice.

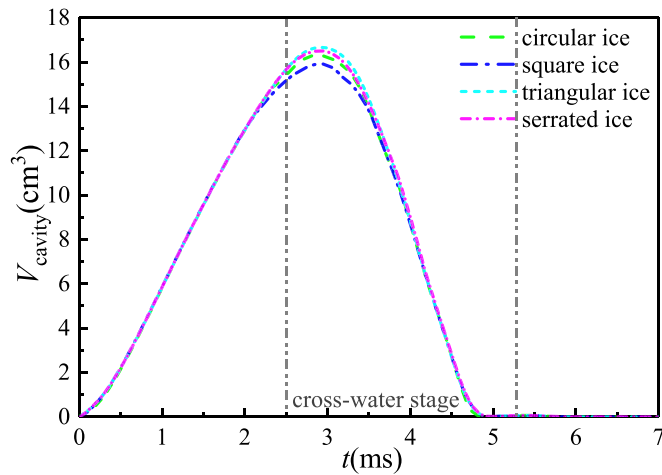


Fig. 29. The volume change of cavity under different shapes of floating ice.

arch" free liquid surface expands to the sides with more fluid, resulting in the surface of the vehicle on the far-ice side being less likely to be wet. The evolution of the tail cavity in different ice thicknesses remains consistent, indicating that the ice thickness primarily affects the development of the shoulder cavity and free liquid surface while having little effect on the tail cavity. With thicker ice floes, upward-moving fluid particles at the water surface continue to be obstructed by the ice, resulting in splashes to both sides and a more pronounced water column

(Fig. 19, 5.8–6.8 ms). During the cross-water stage of the vehicle, the attenuation degree of cavity increases slightly with the thickness of ice, and the attenuation time slightly advances with the thickness of ice.

4.2.2. The deflection attitude change of floating ice with different thickness and motion characteristics of the vehicle

The floating ice undergoes overturning and spreading due to the action of fluid force during the water exit, which causes a change in its attitude. Fig. 22a–b depicts the deflection angle and the deflection angular velocity of the ice around the z-axis during water exit, respectively, in which the counterclockwise rotation (outward deflection) around the z-axis is defined as the positive direction.

It is evident that the deflection of the ice becomes more prominent as the vehicle approaches the water surface. The deflection of ice primarily occurs during the cross-water stage and the stage of emerging from the water surface, and the deflection attitude of floating ice with different thicknesses varies greatly. The ice with a thickness of $0.5 D_0$, having the minimum weight and inertia, experiences a substantial influence from fluid forces, resulting in the largest deflection angle. During the motion of the vehicle, ice floes less than $1.5 D_0$ maintain an outward deflection, and the deflection angle rapidly decreases with the thickness of the ice. However, ice floes with a thickness of $2.0 D_0$ deflect inwardly slightly and then outwardly slightly. This indicates that when the thickness of the ice exceeds a certain critical value, due to their large weight and inertia, ice floes are less affected by the fluid force and exhibit a different deflection attitude during water exit compared to ice floes with thicknesses less than the critical value.

The curves of the vertical and horizontal velocity as well as the displacement of the floating ice during water exit are provided in Fig. 23. It is apparent that, before the vehicle emerges from the water, the vertical velocity and displacement decrease as the thickness of the floating ice increases, which can be attributed to the greater weight and inertia of thicker ice. Moreover, as the thicker floating ice contacts the cavity earlier, its starting time of motion is advanced. In the horizontal direction, the ice floe initially moves outward and subsequently inward. Both the horizontal velocity and displacement exhibit an increasing trend with ice thickness. This can be attributed to the larger volume of thicker floating ice submerged in water, causing the outward-flowing fluid has a larger area of action on the side wall of the ice and a longer action time during the process of water exit of the vehicle. Consequently, the ice floe gains more horizontal kinetic energy. After the vehicle exits the water surface, the upward-moving viscous fluid particles near its tail still possess a certain speed. The fluid particles in the far field converge towards the water exit point and move upward, while driving the floating ice to move inward. Due to the minimum weight and inertia of the $0.5 D_0$ ice, its inward displacement is more obvious.

Fig. 24a–c depicts the variations in the vertical and horizontal velocity as well as pitch angle around the z-axis of the vehicle under different thicknesses of floating ice. It is observed that, upon the collapse

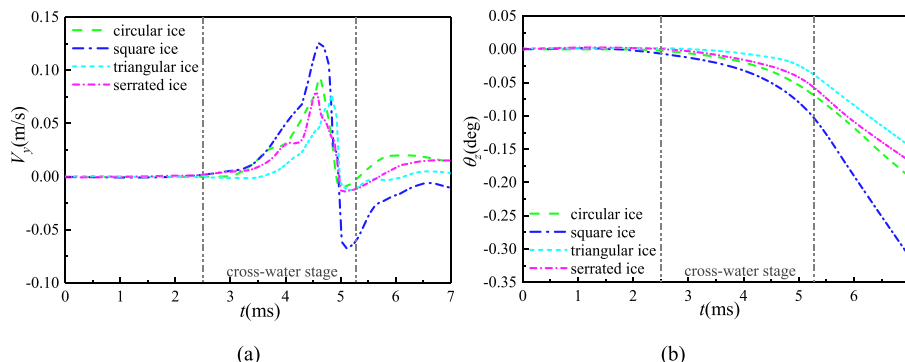


Fig. 30. The motion stability of the vehicle under different shapes of floating ice: (a) horizontal velocity; (b) pitch angle change around the z-axis.

of the tail cavity, a portion of the energy is absorbed by the thicker ice floes. Consequently, the kinetic energy acquired by the vehicle decreases as the ice thickness increases, leading to a lower vertical velocity after emerging from the water. During the cross-water stage and subsequent exit from the water surface, the horizontal velocity and pitch angle around the z -axis increase with increasing thickness. The underlying reason for this phenomenon is that thicker ice floes cause the vehicle to wet earlier, and the fluid collides with the surface of the ice floe, resulting in a rebound effect, which not only wets the surface of the vehicle but also transfers a portion of the kinetic energy to it. The duration of this process is longer for thicker ice floes, which consequently has a greater impact on the stability of the vehicle's motion.

4.3. Influence of the shape of floating ice on the water-exit cavity evolution and motion stability of the vehicle

Based on the analysis of the circular floating ice of **1 ice** in the above chapters, keeping the thickness D_0 , characteristic length $2.0 D_0$, and initial radial gap between the ice and the edge of the vehicle of $0.125 D_0$ unchanged. From the perspective of smoothness, plane, acute angle and approximate irregularity, circular ice, square ice, triangular ice and serrated ice are established in turn, so as to explore the influence of different floating ice shapes on the cavity evolution and motion characteristics of the vehicle. The top view of the distribution of ice floes with different shapes is shown in Fig. 25.

Figs. 26 and 27 are the front view and side view of the three-dimensional water-exit cavity evolution corresponding to circular ice, square ice, triangular ice and serrated ice, respectively. Additionally, Figs. 28 and 29 present the wetting degree of the vehicle and the volume change of cavity under different shapes of floating ice, respectively. The influence of different shapes of floating ice on the cavity and the wetting of the vehicle begins to be reflected during the cross-water stage. As the vehicle continues to rise, the differences between different ice shapes become more obvious.

The degree of influence from floating ice on the cavity is highest for square ice due to the maximum contact area between the cavity and the side wall of the ice. The height of the near-ice side "circular arch" free surface is the highest and relatively smooth (Figs. 26 and 27, 3.4–4.6 ms), and the earliest wetting of the vehicle occurs, with the highest degree of wetting and the lowest peak cavity volume. In contrast, the influence of the triangular ice on the cavity is the least. This is because only the sharp-edged portion of the triangular ice is closest to the cavity, resulting in the smallest contact area between the wall surface and the cavity. As a result, the change in the cavity and the free surface of the triangular ice is minimal. This is evident in the lower height of the "circular arch" free surface (Fig. 27, 3.4 ms), the smaller wetting area of the vehicle on the near-ice side, and the highest peak cavity volume (Fig. 29). The serrated ice, with its complex shape and sharp edges similar to those of triangular ice, leads to a delayed wetting of the vehicle. The presence of multiple raised edges increases the contact area with the cavity and the free liquid surface, which falls between that of triangular and circular ice. This results in a varying degree of wetting of the vehicle after detachment from the water surface, from high to low: square ice, circular ice, triangular ice, and serrated ice. Overall, the degree of influence from floating ice on the cavity varies depending on the ice type, with square ice exerting the highest influence, while triangular and serrated ice have less impact.

Fig. 30 illustrates the influence of different ice floe shapes on the motion stability of the vehicle. The square ice floe, due to its larger contact area with the cavity and the side wall of the floating ice, results in a higher wetting degree of the vehicle on the near-ice side. Consequently, it has a more significant influence on the vehicle's horizontal velocity and pitch angle change around the z -axis. Conversely, the triangular ice floe has the least contact area between the floating ice wall and the cavity, leading to minimal impact on the vehicle's horizontal velocity and pitch angle change around the z -axis.

5. Conclusions

In this paper, the mechanisms of the influence of floating ice on the water-exit cavity evolution and the motion characteristics of the vehicle were explored by comparing and analyzing the underwater and cross-water stages of the vehicle under varying quantities, thicknesses and shapes of floating ice. The key findings can be summarized as follows:

- (1) Due to the obstruction of floating ice, the cavity on the near-ice side becomes bent and deformed, accelerating the contraction and collapse of the cavity. This results in a "circular arch" shape of the free liquid surface, causing premature wetting of the vehicle. Additionally, floating ice disrupts the uniformity of the water layer on the upper surface of the vehicle. As a result, the vehicle's surface on the far-ice side is not fully covered, leading to a decreased wetting degree. The wetting degree of the vehicle's surface after complete emergence from the water increases with increasing quantity and decreases with increasing thickness of floating ice. The turning point of the wetting curve advances with the increasing quantity and thickness of ice. The degree of influence from floating ice on the cavity varies depending on the ice type, with square ice exerting the highest influence, while triangular and serrated ice have less impact.
- (2) Floating ice reduces the volume of vapor and its impact on cavitation increases with the quantity. Moreover, it alters the distribution of velocity fields and vortex structures. On the near-ice side, the high-speed zones and vortex zones exhibit a larger extent due to the presence of floating ice.
- (3) In the direction of the ice, the hydrodynamic force and moment acting on the vehicle are stronger, with more drastic changes and longer fluctuation durations. In situations where a small amount of floating ice exists around the water-exit point, the vertical velocity of the vehicle after leaving the water surface is slightly higher than that of an ice-free environment. When the floating ice is asymmetrically distributed around the water-exit point, the horizontal velocity of the vehicle is greatly disturbed, leading to greater deviations in both horizontal velocity and attitude angle. The vertical velocity of the vehicle exiting from the water decreases with increasing thickness, while the horizontal velocity and pitch angle around the z -direction increase with increasing thickness.

CRedit authorship contribution statement

Hao Wang: Writing – review & editing, Writing – original draft, Software, Methodology, Investigation, Formal analysis, Conceptualization. **Zhengui Huang:** Writing – review & editing, Project administration, Conceptualization. **Xiaowei Cai:** Supervision, Investigation. **Xiangyan Liu:** Visualization. **Zhihua Chen:** Conceptualization. **Xiaodong Na:** Data curation.

Declaration of competing interest

The authors declare that they have no known competing financial interests or personal relationships that could have appeared to influence the work reported in this paper.

Data availability

The authors are unable or have chosen not to specify which data has been used.

Acknowledgments

This research is supported by the National Natural Science Foundation of China (No. 12002165). We are grateful for the support.

Appendix A. Supplementary data

Supplementary data to this article can be found online at <https://doi.org/10.1016/j.oceaneng.2024.117374>.

References

- Brennen, C.E., 1995. *Cavitation and Bubble Dynamics*. Oxford University, New York, NY, USA.
- Brennen, C.E., 2013. *Cavitation and Bubble Dynamics*. Cambridge University Press.
- Chen, S.R., Shi, Y., Pan, G., Gao, S., 2021. Experimental research on cavitation evolution and movement characteristics of the projectile during vertical launching. *J. Mar. Sci. Eng.* 9 (12), 1359.
- Chen, Y., Li, J., Gong, Z.X., Chen, X., Lu, C.J., 2021. LES investigation on cavitating flow structures and loads of water-exiting submerged vehicles using a uniform filter of octree-based grids. *Ocean Eng.* 225, 108811.
- Cui, W.Z., Zhang, S., Zhang, Q., Sun, T.Z., 2023. Dynamic characteristics of unsteady cavity evolution of high-speed projectiles passing through holes in free surface ice flows. *Phys. Fluids.* 35 (9), 095126.
- Fu, G.Q., Zhao, J.L., Sun, L.P., Yang, L., 2018. Experimental investigation of the characteristics of an artificial cavity during the water-exit of a slender body. *J. Mae Sci Appl.* 17 (4), 578–584.
- Guo, R., Sun, T.Y., 2020. The arctic strategy under ROK's "new northern policy": process and constraints. *J. Int. Relat.* (3), 136–153, 159.
- Huang, B., Zhao, Y., Wang, G.Y., 2014. Large eddy simulation of turbulent vortex–cavitation interactions in transient sheet/cloud cavitating flows. *Comput. Fluids.* 92 (20), 113–124.
- Hao, H.H., Song, Y.P., Yu, J.Y., Chen, F., Liu, T., 2019. Numerical analysis of water exit for a sphere with constant velocity using the lattice Boltzmann method. *Appl. Ocean Res.* 84 (12), 163–178.
- Kunz, R.F., Boger, D.A., Stinebring, D.R.A., 2000. Preconditioned Navier-Stokes method for two-phase flows with application to cavitation prediction. *Comput. Fluid.* 29 (8), 849–875.
- Korobkin, A., 2013. A linearized model of water exit. *J. Fluid Mech.* 737, 368–386.
- Logvinovich, G.V., 1969. *Hydrodynamics of Flows with Free Boundaries*. Naukova Dumka, Kiev.
- Liu, T.T., Huang, B., Wang, G.Y., Zhang, M.J., 2017. Numerical investigation of ventilated cavitating flows around a vertical underwater-launched projectile. *Astronautical Systems Engineering Technology.* 1 (4), 22–28.
- Menter, F.R., 1994. Two-equation eddy-viscosity turbulence models for engineering applications. *J. AIAA Journal.* 32 (8), 1598–1605.
- Moyo, S., Greenhow, M., 2000. Free motion of a cylinder moving below and through a free surface. *Appl. Ocean Res.* 22 (1), 31–44.
- Moore, G.W.K., Howell, S.E.L., Brady, M., Xu, X., McNeil, K., 2021. Anomalous collapses of Nares Strait ice arches leads to enhanced export of Arctic sea ice. *Nat. Commun.* 12 (1), 1–8.
- Nam, J.H., Park, I., Lee, H.J., Kwon, M.O., Choi, K., Seo, Y., 2013. Simulation of optimal Arctic routes using a numerical sea ice model based on an ice-coupled ocean circulation method. *Int. J. Nav Arch Ocean.* 5 (2), 210–226.
- Nguyen, V., Phan, T., Duy, T., Park, W., 2022. Unsteady cavitation around submerged and water-exit projectiles under the effect of the free surface: a numerical study. *Ocean Eng.* 263, 112368.
- Quan, X.B., Li, Y., Wei, H.P., Lv, H.B., Xin, W.Q., Lu, C.J., 2008. Cavitation collapse characteristic research in the out-of-water progress of underwater vehicles. *J. Ship Mech.* 12 (4), 545–549.
- Sauer, J., Schnerr, G.H., 2001. Development of a new cavitation model based on bubble dynamics. *Z. Angew. Math. Mech.* 81 (S3), S561–S562.
- Sun, T., Zhang, X., Xu, C., Zhang, G., Jiang, S., Zong, Z., 2019. Numerical modeling and simulation of the shedding mechanism and vortex structures at the development stage of ventilated partial cavitating flows. *Eur. J. Mech. B Fluid.* 76, 223–232.
- Shi, Y., Gao, S., Pan, G., Quan, X.B., 2022. Simulation of the wake vortex and trajectory characteristics of successively launched multiple projectiles. *Ocean Eng.* 249, 110962.
- Sun, L.Q., Ren, Z.Y., Li, Z.P., Ma, G.H., Zhao, J.Z., 2022. Prediction of probability of successful water-exit for underwater vehicles under wave action. *J. Natl. Univ. Def. Technol.* 44 (5), 134–141.
- Sun, T.Z., Zhang, J.Y., Wei, H.P., Zhang, D., Zhang, G.Y., 2022. Experimental investigation of the influence of floating ices constraint on the cavity dynamics of an axisymmetric body during the water exit process. *Ocean Eng.* 244, 110383.
- Takamura, K., Uchiyama, T., 2021. Calculation model for water mass entrained by the water exit of a particle using two projected images captured from orthogonal directions. *Ocean Eng.* 266, 112848.
- Wang, Y., Huang, C., Fang, X., Wu, X., Du, T., 2016. On the internal collapse phenomenon at the closure of cavitation bubbles in a deceleration process of underwater vertical launching. *Appl. Ocean Res.* 56, 157–165.
- Wang, H., Huang, Z.G., Huang, D., 2022a. Influences of floating ice on the vertical water entry process of a trans-media projectile at high speeds. *Ocean Eng.* 265, 112548.
- Wang, H., Luo, Y.C., Chen, Z.H., Guo, Z.Q., Huang, Z.G., 2022b. Influences of ice-water mixture on the vertical water-entry of a cylinder at a low velocity. *Ocean Eng.* 256, 111464.
- Wang, H., Huang, Z.G., Guo, Z.Q., 2023. Numerical study on the influence of floating ice on the water-exit hydrodynamic characteristics of a trans-media vehicle. *J. Phys.: Conf. Ser.* 2478, 112008.
- Xu, H., Wei, Y., Wang, C., Lu, J., 2019. On wake vortex encounter of axial-symmetric projectiles launched successively underwater. *Ocean Eng.* 189, 106382.
- You, C., Sun, T.Z., Zhang, G.Y., Wei, Y.J., Zong, Z., 2022. Numerical study on effect of brush ice on water exit dynamics of ventilated cavitation cylinder. *Ocean Eng.* 245, 110443.
- Zhao, J.L., Guo, B.S., Sun, L.Q., Yao, X.L., 2016. Experimental study on oblique water-exit of slender bodies. *Explos. Shock Waves.* 36 (1), 113–120.
- Zhang, N., Wang, J., Wu, Y.S., Wang, K., Zhang, Q.H., Wu, S.Q., You, Z.J., Ma, Y.T., 2019. A modelling study of ice effect on tidal damping in the Bohai Sea. *Ocean Eng.* 173, 748–760.
- Zhang, G.Y., You, C., Wei, H.P., Sun, T.Z., Yang, B.Y., 2021. Experimental study on the effects of brush ice on the water-exit dynamics of an underwater vehicle. *Appl. Ocean Res.* 117, 102948.
- Zhao, Q.K., Chen, T., Wei, X., Chen, X.B., Yao, X.L., Wang, W.P., 2022. Research on the characteristics of cavitation flow and pressure load during vertical water exit of different head-shaped vehicles. *Ocean Eng.* 265, 112663.